

Charge-Carrier Cooling and Polarization Memory Loss in Formamidinium Tin Triiodide

Kimberley J. Savill,[†] Matthew T. Klug,[†] Rebecca L. Milot,[‡] Henry J. Snaith,[†] and
Laura M. Herz^{*,†}

*Department of Physics, University of Oxford, Clarendon Laboratory, Parks Road, Oxford OX1
3PU, U.K., and Department of Physics, University of Warwick, Gibbet Hill Road, Coventry, CV4
7AL, UK.*

E-mail: laura.herz@physics.ox.ac.uk

*To whom correspondence should be addressed

[†]Department of Physics, University of Oxford, Clarendon Laboratory, Parks Road, Oxford OX1 3PU, U.K.

[‡]Department of Physics, University of Warwick, Gibbet Hill Road, Coventry, CV4 7AL, UK.

Contents

1	Experimental details	3
1.1	Sample fabrication	3
1.2	Sample characterisation methods	3
1.3	Spectroscopic techniques	4
1.4	Details of excitation density calculations	6
2	Film characterisation	7
3	Absorbance data	9
4	Determining carrier temperature from measured spectra	9
4.1	Approaches used previously	10
4.2	Choice of model used in this work	12
4.3	Impact of broadening	15
4.4	Impact of accounting for the joint density of states	21
4.5	Fitting procedure and results	25
5	Additional PL decay curves	34
6	Polarization anisotropy measurements	35

1 Experimental details

1.1 Sample fabrication

Formamidinium Iodide (FAI) was purchased from Greatcell Solar. Tin (II) iodide (SnI_2 , 99.999% Ultradry) was purchased from Alfa Aesar. Tin (II) fluoride (SnF_2 , 99%), n,n-dimethylformamide (DMF, anhydrous, $\geq 99.8\%$), dimethyl sulfoxide (DMSO, anhydrous, $\geq 99.9\%$), diethyl ether (anhydrous, $\geq 99.7\%$) was purchased from Sigma Aldrich. A stoichiometric 1.0 M solution of FASnI_3 was prepared in a nitrogen atmosphere by dissolving FAI and SnI_2 in a mixed solvent of 4:1 DMF:DMSO by volume. An additional amount of SnF_2 (5% molar amount with respect to SnI_2) was dissolved in the solution. The solution was stirred overnight at room temperature and filtered with a 0.45 μm PTFE filter prior to use. The PL samples were prepared in a nitrogen atmosphere by statically dispensing the solution on an O_2 -plasma treated quartz disc and spincoating at 4 krpm for 30 s with a 6 s ramp. At 12 s from the start of the spincoating program, 200 μL of diethyl ether is dropped onto the spinning film, which causes the perovskite film to immediately darken. The films are subsequently annealed at 70 $^\circ\text{C}$ for 20 minutes in an N_2 atmosphere.

1.2 Sample characterisation methods

Film thickness was measured at several positions across a single sample on quartz substrate using a Veeco Dektak 150 surface profilometer to give an average thickness of 345 ± 15 nm (see Table S1 below). For scanning electron microscopy and x-ray diffraction measurements O_2 -plasma treated TEC15 fluorine-doped tin oxide substrates were used in place of quartz. Thin films of FASnI_3 with 5% SnF_2 were prepared on these FTO substrates following the method described above. A Hitachi S-4300 scanning electron microscope was used to obtain SEM images, with acceleration voltage 10 kV and probe current 11 μA . A Rigaku SmartLab X-ray diffractometer was used to obtain XRD spectra, with $\text{CuK}\alpha_1$ (1.54060 \AA) and a HyPix-3000 2D hybrid pixel array detector.

1.3 Spectroscopic techniques

Steady state absorption: The optical absorbance spectrum of our thin films was taken with a Bruker Vertex 80v Fourier-transform infrared spectrometer, fitted with a transmission/reflection accessory and using a silicon diode detector. A tungsten halogen lamp was used as the source. Samples for this measurement were mounted in a gas exchange cryostat (Oxford Instruments, OptistatCF2) with temperature controller (Oxford Instruments, MercuryITC) allowing resistive heating and liquid helium cooling. Here we focus on measurement at 295 K only.

Photoluminescence upconversion spectroscopy: Samples kept in a nitrogen-filled glovebox were loaded into a vacuum cell before removal from the glovebox, and then placed under vacuum with continuous pumping to maintain pressure at 2.5×10^{-3} mbar or lower while spectroscopic measurements were performed, to minimise possible exposure to air. For upconversion spectroscopy, excitation pulses (80 fs length) at a wavelength of 730 nm were generated by a tunable Ti:Sapphire laser (Mai Tai, Spectra Physics) with 80 MHz repetition rate. A half-waveplate and vertical polarizer were used to attenuate the excitation power to 12 mW or 60 mW, with measured beam area of 0.02 mm^2 at the sample position giving excitation fluences of $0.75 \mu\text{J cm}^{-2}$ and $3.75 \mu\text{J cm}^{-2}$ respectively. The corresponding initial charge-carrier pair (electron and hole) densities, averaged across the film thickness, are $6.9 \times 10^{16} \text{ cm}^{-3}$ for the low power condition, and $3.4 \times 10^{17} \text{ cm}^{-3}$ for the high power condition (see calculations in section 1.4). The experimental setup used for time resolved measurements by upconversion has been previously described,^{1,2} with the essential features as follows. Photoluminescence (PL) from the sample was overlapped in a beta-barium borate (BBO) crystal with a vertically polarized gate beam pulse which has a variable time delay with respect to the excitation beam pulses. The upconverted (sum frequency) light leaving the crystal was focussed through a variable-width entry slit into a grating monochromator (Triax, Horiba) and the dispersed signal was detected with a nitrogen-cooled silicon charge coupled device (Symphony, Horiba). Background was reduced using long-pass and bandpass filters chosen to block the excitation before the BBO crystal, as well as the unaltered photoluminescence and gate wavelengths

after the crystal, while allowing upconverted signal to pass. A spectral response correction was applied to all measured spectra, using a tungsten filament lamp with known spectrum. Instrument response measurements, as previously reported, identify a temporal resolution of 270 fs.³ For polarization anisotropy measurements, the polarization of the excitation pulse was varied using a Glan-Thompson polarizer, with power at the sample kept constant between polarizations by adjustment of the half-waveplate. Measurements both perpendicular and parallel to the polarization of the excitation pulse were then taken, using the inherent polarization selectivity of the upconversion process to the gate pulse polarization and crystal geometry.

Time-correlated single photon counting: The setup used for time-correlated single photon counting (TCSPC) measurements was as described for PL upconversion above except for the following: The BBO crystal was removed, and photoluminescence from the sample was directed through a second exit port of the monochromator to a silicon single photon avalanche diode detector. The gate beam was diverted, no longer crossing the photoluminescence beam path, and detected by a photodiode as the trigger pulse. Stepping of detection wavelength across a range to measure spectra was conducted manually, with spectral response accounted for by pinning the measured traces against corresponding PL upconversion spectra.

Time-integrated photoluminescence: As was done for the time-resolved photoluminescence measurements, samples used to measure time-integrated photoluminescence spectra were kept under vacuum with continuous pumping to pressures of 2.5×10^{-3} mbar or less. Samples were excited at 730 nm with a pulsed laser as described above, and spectra were measured using a grating monochromator (Triax, Horiba) and nitrogen-cooled CCD silicon detector (Symphony, Horiba) with integration time ranging from milliseconds to seconds. Spectral response correction was carried out, using a tungsten filament lamp with known spectrum to measure the instrument response.

1.4 Details of excitation density calculations

The excitation wavelength for our time resolved photoluminescence measurements was 730 nm, with power just in front of the sample position measured to be 12 mW or 60 mW for the high and low fluence conditions respectively. Given a spot size of 0.02 mm^2 measured at the sample position, and known repetition rate of 80 MHz, we calculate excitation fluences as follows:

Pulse energy with 12 mW power is given by

$$\frac{12 \times 10^{-3} \text{ W}}{80 \times 10^6 \text{ Hz}} = 1.5 \times 10^{-10} \text{ J}$$

from which excitation fluence fl for each pulse is

$$\begin{aligned} fl &= \frac{1.5 \times 10^{-10} \text{ J}}{2 \times 10^{-4} \text{ cm}^2} = 7.5 \times 10^{-7} \text{ J cm}^{-2} \\ &= 0.75 \mu \text{ J cm}^{-2} \end{aligned}$$

Then for 730 nm excitation, photon energy E is

$$\begin{aligned} E &= \frac{6.626 \times 10^{-34} \text{ Js} \times 2.998 \times 10^8 \text{ m s}^{-1}}{730 \times 10^{-9} \text{ m}} \\ &= 2.721 \times 10^{-19} \text{ J} \end{aligned}$$

As shown in Table S1 below, film thickness d for our FASnI_3 samples is 345.2 nm. The absorbance, calculated from transmittance T and reflectance R as $A = -\ln\left(\frac{T}{1-R}\right)$ and plotted in Figure S3 below, is 1.98 at the excitation wavelength of 730 nm and so the absorption coefficient α is given by:

$$\begin{aligned} \alpha &= \frac{1.98}{345.2 \times 10^{-9} \text{ m}} \\ &= 5.736 \times 10^4 \text{ cm}^{-1} \end{aligned}$$

Assuming one charge-carrier pair is generated for each photon, the initial excitation density of either electrons or holes for an excitation power of 12 mW is:

- $n_0^{\text{front}} = \frac{fl \times \alpha}{E} = 1.6 \times 10^{17} \text{ cm}^{-3}$ at the front surface of the film
- $n_0^{\text{back}} = \frac{fl \times \alpha}{E} \times \exp(-\alpha d) = 2.2 \times 10^{16} \text{ cm}^{-3}$ at the back surface of the film
- $n_0^{\text{average}} = \frac{fl \times (1 - \exp(-\alpha d))}{dE} = 6.9 \times 10^{16} \text{ cm}^{-3}$ averaged across the film

Similarly, for 60 mW excitation power and therefore $3.75 \mu\text{J cm}^{-2}$ fluence, the corresponding values are:

- $n_0^{\text{front}} = 7.9 \times 10^{17} \text{ cm}^{-3}$ at the front surface of the film
- $n_0^{\text{back}} = 1.1 \times 10^{17} \text{ cm}^{-3}$ at the back surface of the film
- $n_0^{\text{average}} = 3.4 \times 10^{17} \text{ cm}^{-3}$ averaged across the film

2 Film characterisation

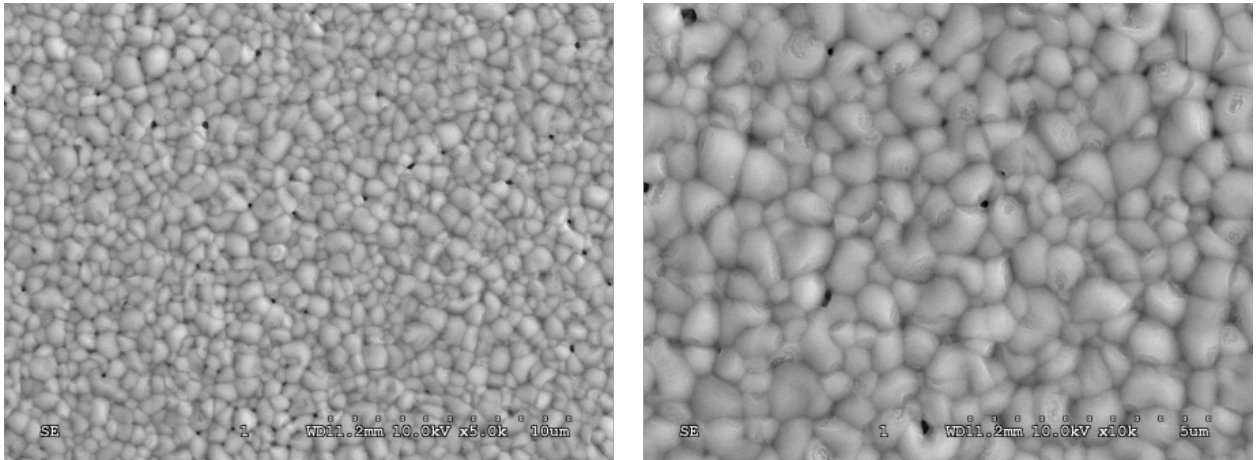


Figure S1: SEM micrographs of FASnI_3 film prepared on FTO substrate, with 5% SnF_2 added during preparation.

Table S1: Thickness of FASnI_3 films with 5% SnF_2 , determined by measurements at four different positions across a typical sample on quartz substrate using a Veeco Dektak 150 surface profilometer.

Position	Thickness (nm)	
Left side	337.8	
Centre 1	338.1	
Centre 2	367.1	
Right side	337.8	
	Mean	Standard Deviation
	345.2	14.6

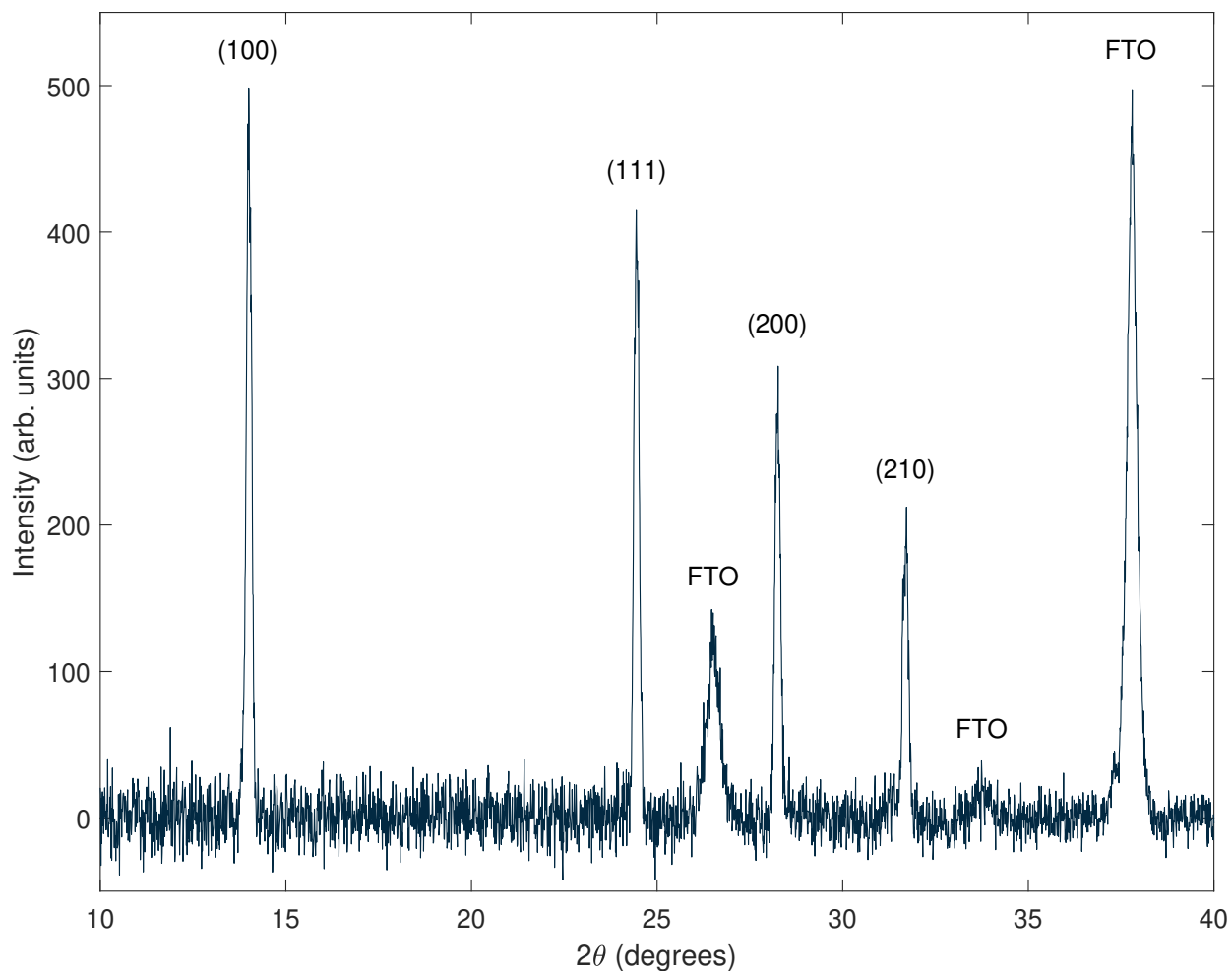


Figure S2: X-ray diffraction pattern for a FASnI_3 film, prepared with 5% SnF_2 added, on FTO substrate. Measurement was performed under vacuum with a Rigaku Diffractometer, at room temperature.

3 Absorbance data

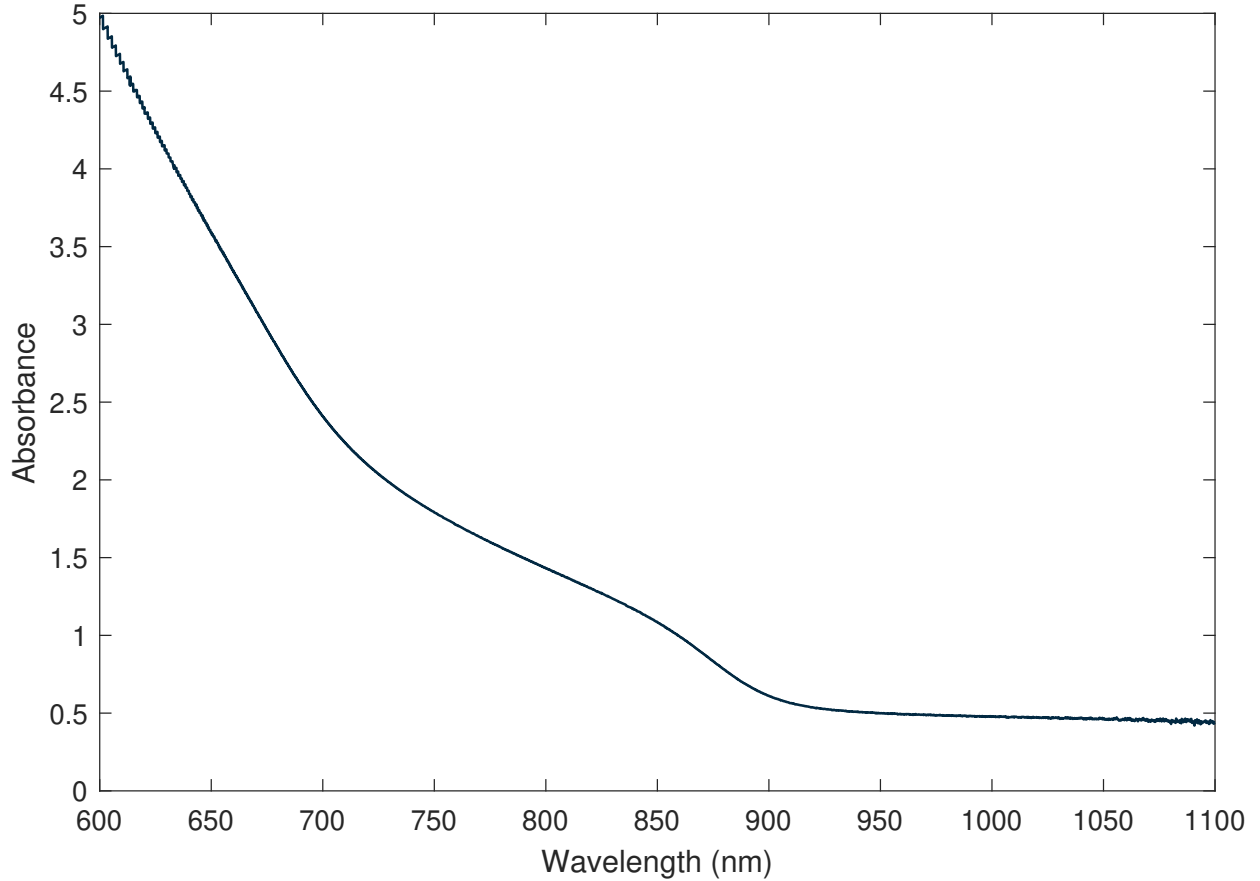


Figure S3: Absorbance spectrum of a FASnI₃ film with 5% SnF₂ added during fabrication, on quartz substrate, measured at 295 K.

4 Determining carrier temperature from measured spectra

Following excitation above the bandgap, the population of excited carriers with excess kinetic energy rapidly thermalizes with itself, although not with the lattice, to give a distribution characterised by a temperature T_c . This temperature can be determined by fitting to the photoluminescence spectrum, which reflects the energetic distribution of charge-carriers undergoing radiative recombination. We use the following model to determine the charge-carrier temperature from the line shape I_{measured} of the emitted PL, with $E = \hbar\omega$ the energy of emitted photons:

$$I_{\text{measured}}(E) = I_{PL}(E) \otimes f(E) \quad (\text{S1})$$

$$I_{PL}(E) \propto \begin{cases} (E - E_g)^{1/2} \exp\left[\frac{-(E - E_g)}{k_B T_c}\right] & E > E_g \\ 0 & \textit{otherwise} \end{cases} \quad (\text{S2})$$

$$f(E) = \frac{1}{\sigma\sqrt{2\pi}} \exp\left(\frac{-(E - E_g)^2}{2\sigma^2}\right) \quad (\text{S3})$$

where E_g is the bandgap and \otimes denotes the convolution of the underlying emission profile I_{PL} with a function $f(E)$ capturing the broadening of the spectrum, chosen as a Gaussian distribution of width σ . The reasoning for this choice of model, which allows a more accurate determination of carrier temperature than that described in much of the previous literature (section 4.1) is explained in section 4.2. The impact of either accounting for or neglecting spectral broadening, and the joint density of states (JDOS), is then explored in depth in sections 4.3 and 4.4 respectively. Finally, further details of the fitting procedure and typical results are provided in section 4.5.

4.1 Approaches used previously

In many recent studies concerned with carrier cooling in metal halide perovskites, carrier temperature has been determined by exponential fits to a selected ‘tail’ region at the high energy side of the measured emission spectrum.^{4–11} The basis for this approach is that the thermalized carriers follow a Boltzmann distribution as a function of energy above the bandgap, E :

$$f_{\text{Boltz}}(E) = A \exp\left(\frac{-E}{k_B T_c}\right) \quad (\text{S4})$$

and so this equation can be used to fit measured data for a given charge-carrier temperature T_c . In some transient absorption studies, where there is a photoinduced absorption (PIA) signal overlapping with emission in the measured spectrum, a linear combination of Equation S4 with a suitable term f_{PIA} for the absorption is used to fit the selected region of the spectrum with a model of the

form $f(E) = A_1 f_{\text{Boltz}}(E) + A_2 f_{\text{PIA}}(E)$ for probe energy E .^{12–14} The exponential fit approach was also sometimes used in the earlier literature on inorganic semiconductors, such as GaAs, CdS, and GaAs/AlGaAs and InGaAs/GaAs quantum wells.^{15–23} However, as we show here, there are several approximations involved in modelling the emission spectrum by a Boltzmann distribution over this range that lead to inaccuracy.

In fact, some earlier works on inorganic semiconductors recognised this and used more complete models including carrier-temperature dependence to calculate spectra for comparison with measured data.^{24–26} However, at the time much of that research was conducted, fitting directly to measured data with a complete model for emission line shape would have been particularly challenging due to the absence of computing technology suitable for the purpose. Works concerned with probing charge-carrier cooling through fits to time-resolved data therefore commonly approximated to the Boltzmann model, allowing carrier temperature to be determined straightforwardly from the gradient of the high energy side of the PL spectra as a semilog plot.^{15–17,21} Some authors noted the deficiencies of this approximation, for instance that neglecting to account for the density of states leads to deviation from the true temperature value²⁷ or that in comparison to fitting the whole line shape, using the Boltzmann model for a selected tail region overestimates temperature.^{28,29} Nonetheless, exponential fits to the tail continued to be widely used. The growing focus on quantum wells within inorganic semiconductor research furthered this approach in many cases,^{18–20,22,23,30–34} since the joint density of states for electronic transitions between quantum levels in such a system is a constant (energy independent),³⁴ and measured PL linewidths can be less than 1 meV.^{35,36} Consequently, the Boltzmann distribution alone is a good approximation to the line shape of emission spectra from quantum well systems.

Fitting to just the high energy tail of the spectrum with a Boltzmann distribution thus emerged as the most commonly used method for determining carrier temperature. In this context, the continued use of such a method in much of the metal halide perovskite literature may be a natural development. However, neither the computational constraints nor the simplified quantum-well density of states which were significant factors in the choice of model in many previous studies

apply to current work on perovskites. As well as these simplifications becoming less justified in principle, the wide range of reported cooling times, spanning several orders of magnitude^{4,13,37,38} suggests that there may be significant errors between studies. The broadening seen in any measured spectrum, and the associated non-exponential curvature through to high energy, gives further reason to doubt the suitability of a simple Boltzmann model. In this context, careful choice of model to determine carrier temperature and avoid the errors in the simple exponential approximation is therefore particularly important. In the following sections we describe the model used in this work, detail its implementation, and provide a comparison between this model and the Boltzmann approach which illustrates the impact of the commonly assumed approximations.

4.2 Choice of model used in this work

Following excitation above the bandgap, carrier-carrier scattering rapidly redistributes energy, leading to a thermalized population that can be considered to have a characteristic temperature T_c .^{6,39,40} The common choice of a Boltzmann distribution function to describe the carrier distribution follows from this. To fully capture the energetic distribution of charge-carriers that could undergo radiative recombination and so contribute to the measured photoluminescence spectrum, the joint density of states of the material must also be taken into account. First principles calculations for the band structure of lead and tin-based perovskites indicate that both valence and conduction bands are well-approximated as parabolic near the band edge.^{41,42} An indication of the range over which this approximation holds is given by work on MAPbI₃ showing that parabolicity remains up to 250 meV from the band edge,⁴³ corresponding to a temperature of 2901 K which substantially exceeds the range of interest for our work. Therefore, parabolicity can be safely assumed to give the usual joint density of states $JDOS \propto (E - E_g)^{1/2}$ for direct band-to-band transitions between parabolic bands in Equation S2 above.

A representative emission profile given by Equation S2 is shown in Figure S4. The line shape produced by this model closely resembles a Boltzmann distribution cut off to 0 for energies below the bandgap, but the parabolic JDOS factor results in a more gradual onset rather than a vertical

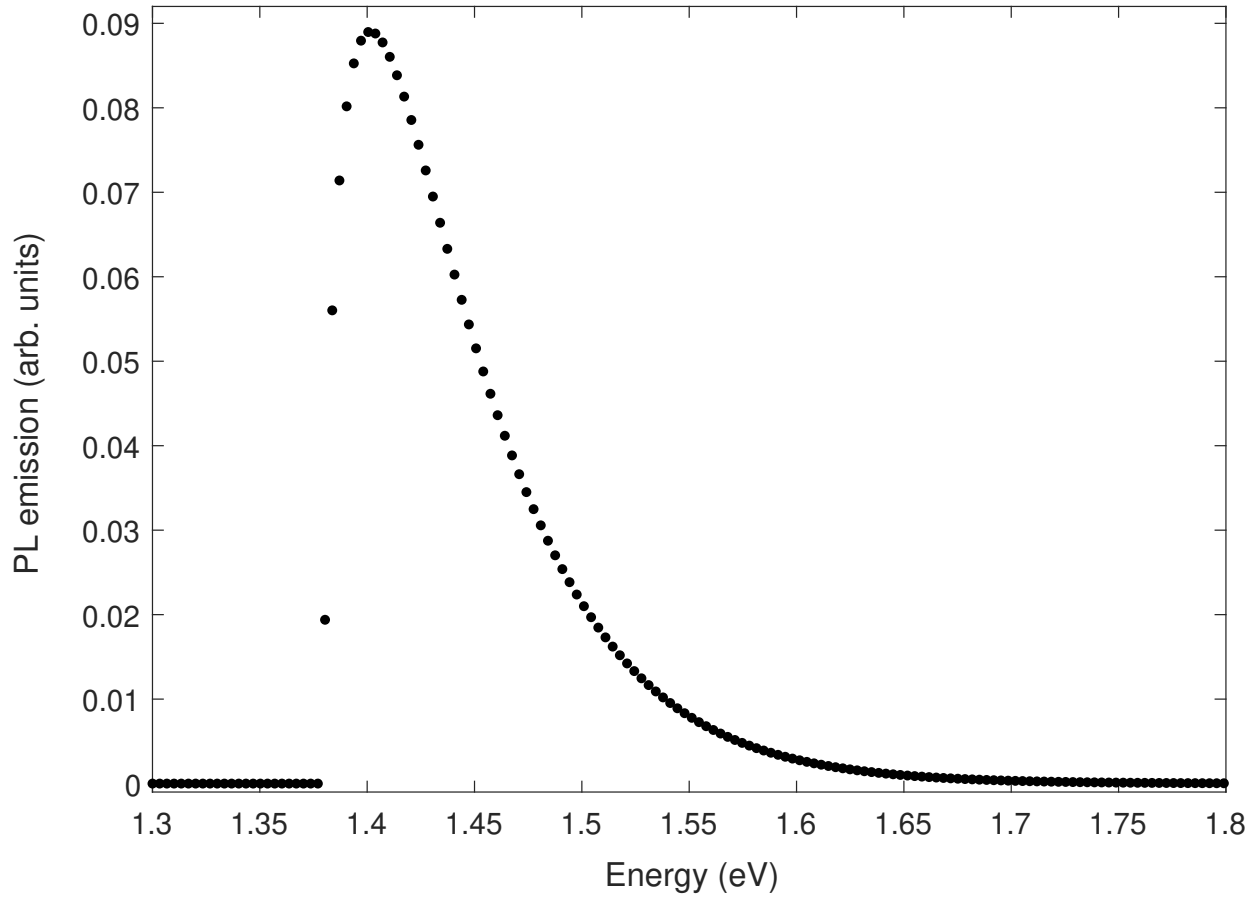


Figure S4: Spontaneous emission profile for a direct gap semiconductor with bandgap 1.38 eV and carrier temperature 500 K, modelled according to Equation S2. Broadening, which would be modelled by convolution with a Gaussian profile as in Equation S1, is not included here.

step, and a less steep decay in intensity moving to high energy than would be seen for a constant density of states. Emission spectra obtained by experiment do not typically show such a defined onset and asymmetrical emission line shape as that shown in Figure S4, being broadened and often closer to symmetrical in appearance. This broadening occurs as a result of factors such as variable lifetime and interactions within the material, with the shape of the spectrum depending upon the underlying mechanism. Carrier coupling to phonons resulting in homogeneous broadening has been identified as the main contributor to broad PL profiles for a variety of lead perovskites^{44–47} and this mechanism has also been suggested for observed broadening in MASnI_3 .⁴⁸ Inhomogeneous broadening, arising from energetic disorder and interactions of charge-carriers with defects and trap states, has also been identified as dominating the line shape of PL spectra for several metal halide perovskite compositions.^{49–52} This is particularly relevant for tin halide perovskites in which the presence of charged tin vacancies can contribute significantly to broadening of the spectrum.⁵³ Spectral broadening can be accounted for when fitting spectra by convolution of I_{PL} with an appropriate choice of function $f(E)$ determined with reference to the shape of measured spectra.

To identify the correct form of the broadening $f(E)$, temperature-independent fits to spectra taken at long delay times after photoexcitation can be examined. As the contribution of hot carriers to the spectrum diminishes with cooling, there is less pronounced variation between the high and low energy sides of the peak at later times whereas the full effects of broadening still remain. Therefore, a model that fits well to these spectra is a good candidate for $f(E)$. Applying this approach to our data, as shown in Figure S5, the late-time line shape is found to be well-described by a Gaussian profile, of the form given in Equation S3 where the width of the peak centered at E_g is determined by the parameter σ , with

$$FWHM = \sqrt{8\ln 2}\sigma \approx 2.35\sigma \quad (\text{S5})$$

giving the full width at half maximum intensity of the peak. A Gaussian line shape is common for

cases where inhomogeneous broadening is significant^{51,54} which is to be expected for tin-based perovskites with a sizeable density of tin vacancies.^{50,53}

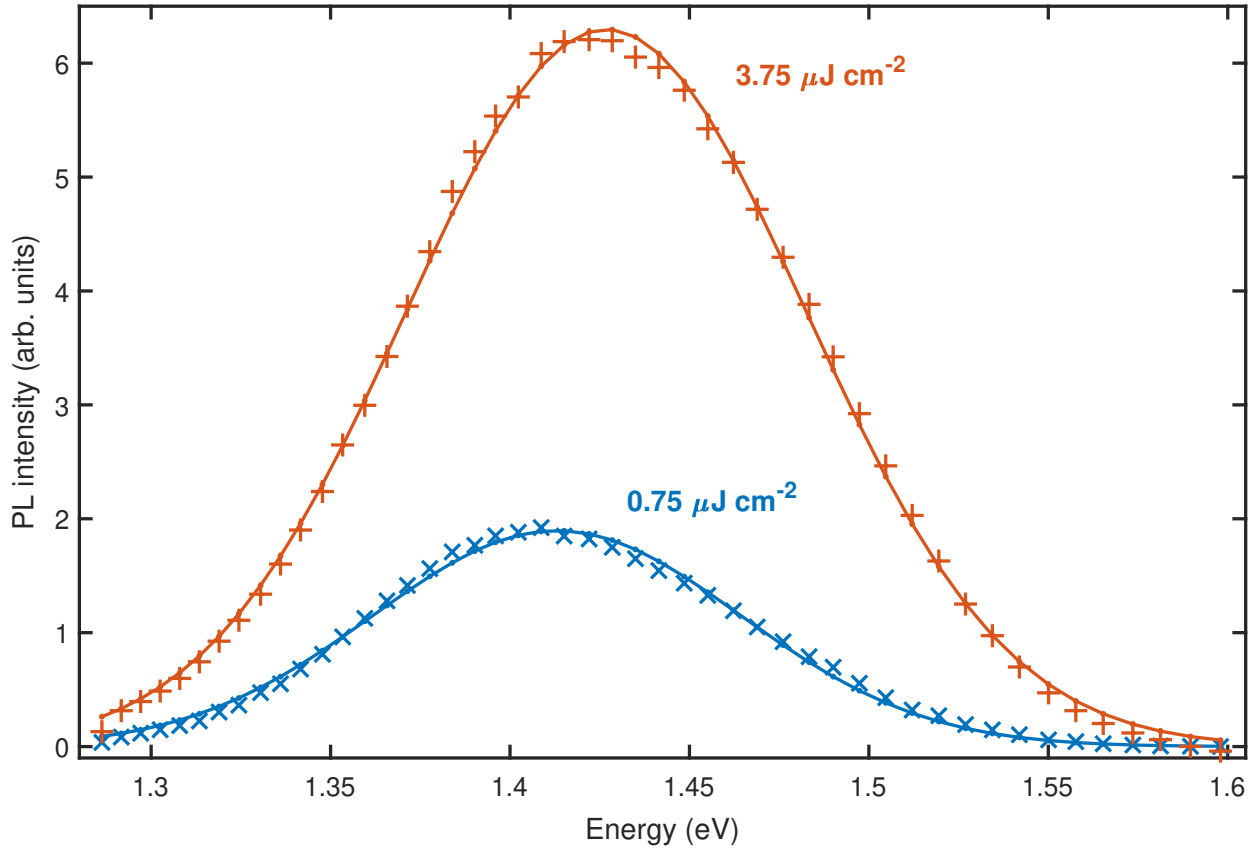


Figure S5: Time resolved PL spectra (+ or × markers) of a FASnI₃ film on quartz, with Gaussian fits (solid lines) illustrating the broadened symmetric spectral profile when there is not a significant contribution from hot carriers. The spectra shown here are averages over several measurements at 100 ps delay time after excitation at 730 nm with fluence as indicated.

The full model given by Equations S1 – S3 thus captures both the broadening effects and the distribution of carriers over the perovskite’s density of electronic states, allowing carrier temperature to be determined from fits to the full measured spectra rather than a selected region at the high energy side only. The impacts of this are discussed in the following sections.

4.3 Impact of broadening

To demonstrate the importance of accounting for spectral broadening when fitting data to extract charge-carrier temperature, the common exponential tail fitting approach can be tested against

spectra modelled with Equations S1 – S3 for known input carrier temperatures. Varying the value of σ in Equation S3 to represent varying amounts of broadening, and comparing fitted to model temperatures, then gives an indication of the impact of broadening on the discrepancy between a full line shape description and the simple Boltzmann model. Spectra calculated using Equations S1 - S3 with σ valued at 43.4 meV, representative of the broadening we see in measured spectra for FASnI₃, are shown in Figure S6A, and similarly calculated spectra with σ value 5 meV for low broadening are shown in Figure S6B. Figure S6C and D show fits to the selected tail region of each spectrum, marked in grey in Figure S6A and B and covering the intensity range from 50% down to 5% of peak emission intensity for each input temperature. Exponential tail fits, plotted as solid lines, can be seen to deviate more from the data points in the tail of calculated spectra with $\sigma = 43.4$ meV (Figure S6C) than $\sigma = 5$ meV (Figure S6D) with the fit also being worse for lower charge-carrier temperatures. Comparing the extracted charge-carrier temperatures from exponential tail fitting against the input temperatures used to calculate the spectra makes the impact of broadening more apparent. In the larger broadening case, fitted charge-carrier temperatures shown in Figure S6E level out to around 300 K as the actual input temperatures drop towards 0 K. Figure S6F, with an order of magnitude lower σ , shows no such pronounced plateau at low charge-carrier temperatures. This indicates that the discrepancy between input and tail fit values for low charge-carrier temperatures is due to spectral broadening, whereas the divergence seen for increasing charge-carrier temperatures with both σ values (explained in Section 4.4) is not.

The reason for substantial overestimation of T_c from exponential tail fits for low charge-carrier temperatures when spectra are broadened is that as carriers cool and T_c drops, the high energy emission from hot carriers decays away and the spectrum becomes more symmetrical, as can be seen in Figure S6A. The shape of the spectrum is then much closer to the broadening profile, in this case a Gaussian, and the shape of the broadening profile over the selected tail region then places a lower limit on the charge-carrier temperature values extracted by exponential fitting. Since neither the broadening function nor the PL spectra at low values of T_c are in fact exponential in profile over any chosen range, the choice of tail region to fit then determines the slope of the fitted

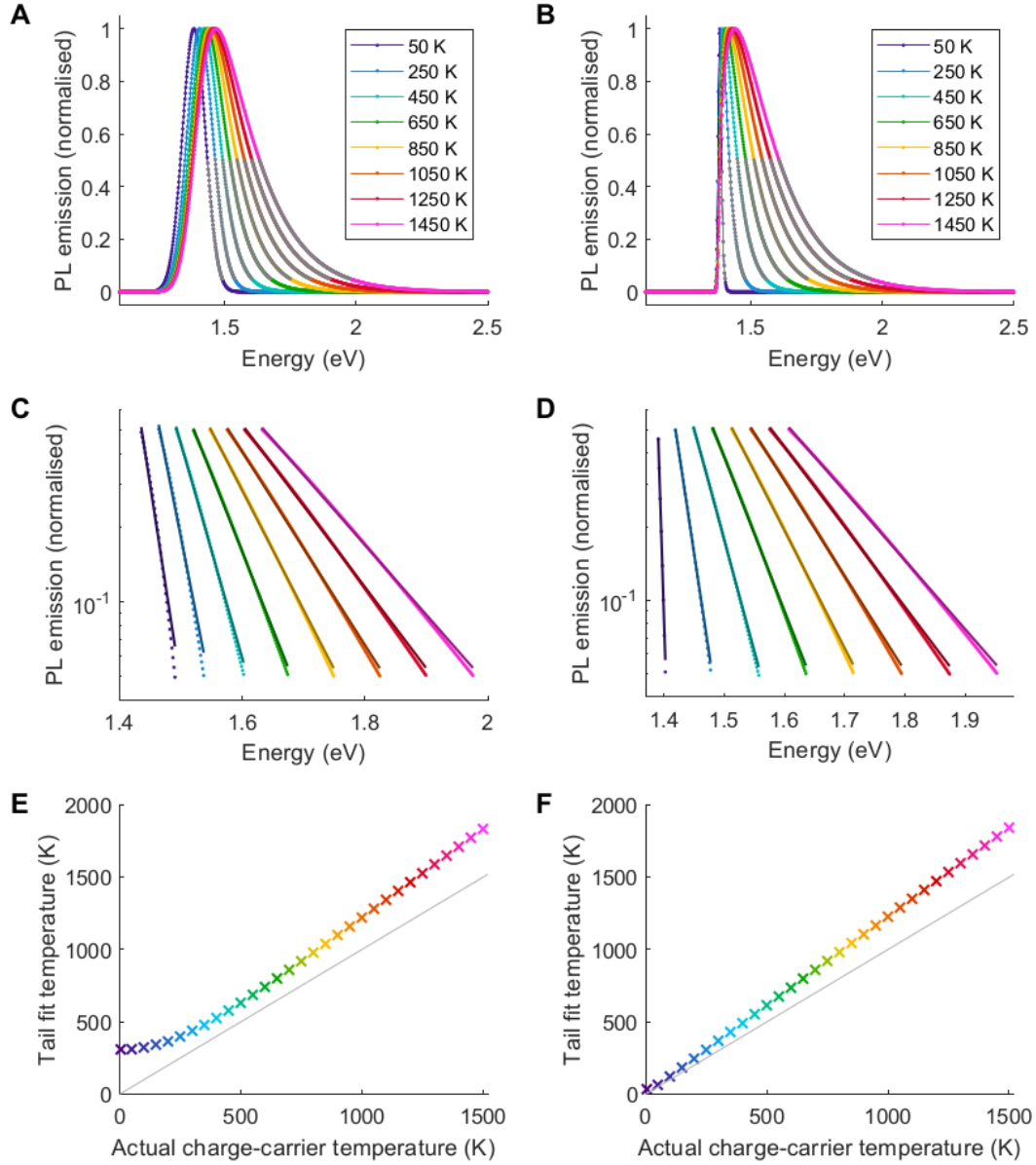


Figure S6: Impact of spectral broadening on charge-carrier temperatures (E, F) extracted from exponential fits (C, D) to a selected tail region of PL spectra (A, B) modelled with Equations S1 - S3, using $E_g = 1.38$ eV. The realistic broadening case (A, C, E) similar to our measured spectra uses $\sigma = 43.4$ meV for modelling, and the low broadening case (B, D, F) uses $\sigma = 5$ meV. A, B) Modelled spectra at the charge-carrier temperatures indicated in the legend, selected at regular intervals across the 5 - 1500 K range. Selected tail regions to fit to are overlaid in grey, covering the range from 50% to 5% of the peak emission amplitude at the high-energy side of each spectrum. C, D) Selected tail regions from the spectra in A and B respectively (point markers) and exponential fits to each (solid lines). E, F) Charge-carrier temperatures extracted from exponential fits to the selected tail regions as shown in C and D respectively. Marker colors match the modelled spectra in A-D. The grey line is a guide to the eye indicating equality between actual input temperature and tail fit temperature.

exponential and consequently how high or low the fitted temperature is. These two points are illustrated by fitting an exponential to selected regions of a Gaussian profile, where as shown in Figure S7 extreme temperature values may be obtained for selected regions near enough to the peak or far enough out in the tail. The temperature to which the carrier population appears to stabilise over time as cooling occurs will therefore depend on where the tail region for fitting is chosen to be. Moreover, as the comparison between Figures S7A and S7B shows, charge-carrier temperatures extracted from tail fits depend upon the length of the selected tail region as well as how far down in intensity from the peak it is chosen to begin. Dependence on the choice of tail region to fit to is also seen for fits against modelled spectra across the temperature range, as Figure S8 shows, with higher values of T_c extracted if a narrower range is chosen, or if the selected tail region lies closer to the peak of the spectrum.

These simulations show that if, similarly, experimental carrier temperatures are determined by fitting to only a selected region of a measured spectrum, the particular choice of tail becomes important. In particular considering the necessary assumption that charge-carrier temperatures ultimately ought to return to the lattice temperature, attempting to select a tail region for which fitted temperatures show this behaviour at late times is then likely to skew results. This problem of dependence on tail selection has been recognised in some previous works, for instance by averaging over fitted temperatures for systematically varying choices of tail region and comparing results with different tail lengths.¹³ Still, in many cases a fixed energy interval is simply used without apparent consideration of other choices. By fitting the whole spectrum with the complete expression given by Equations S1 - S3, we eliminate the problem of dependence on choice of tail region for determining carrier temperature. The inclusion of spectral broadening in our model, which is necessary for a good fit across the full emission profile, then also ensures that the ‘cooler’ spectra with limited hot carrier contribution do not yield dramatically overestimated temperatures.

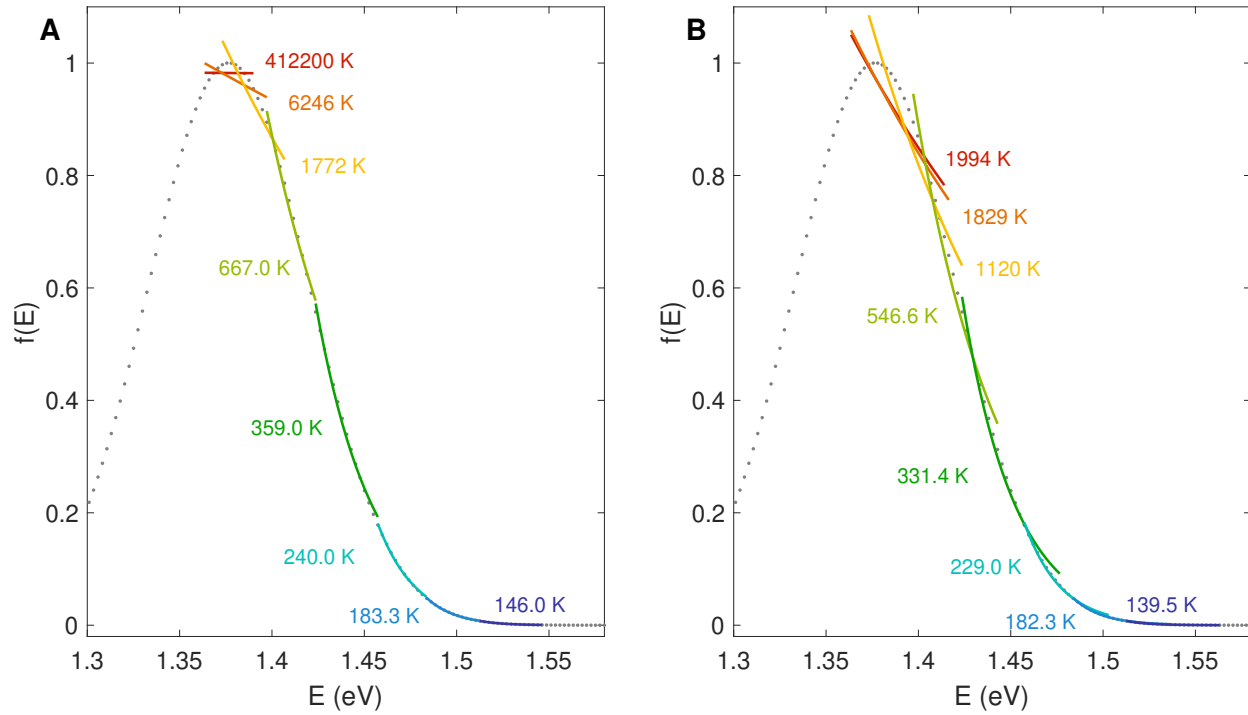


Figure S7: Exponential fits to a Gaussian profile calculated using Equation S3, demonstrating the wide range of ‘temperatures’ extracted when fitting to different selected regions. Point markers show the Gaussian profile with $E_g = 1.38$ eV and $\sigma = 43.4$ meV, the same parameter values used to capture broadening for our measured spectra at $0.75 \mu\text{J cm}^{-2}$ excitation fluence. Solid lines show the exponential fits for eight selected regions each covering a range of 30 meV (A) or 50 meV (B), with extracted ‘temperature’ for each region shown in the same color as the fitted line. The same lower energy bounds, indicated by matching line colors, are used for each of the selected regions in both (A) and (B) to illustrate the impact of using a wider range on the ‘temperature’ extracted from such exponential fits.

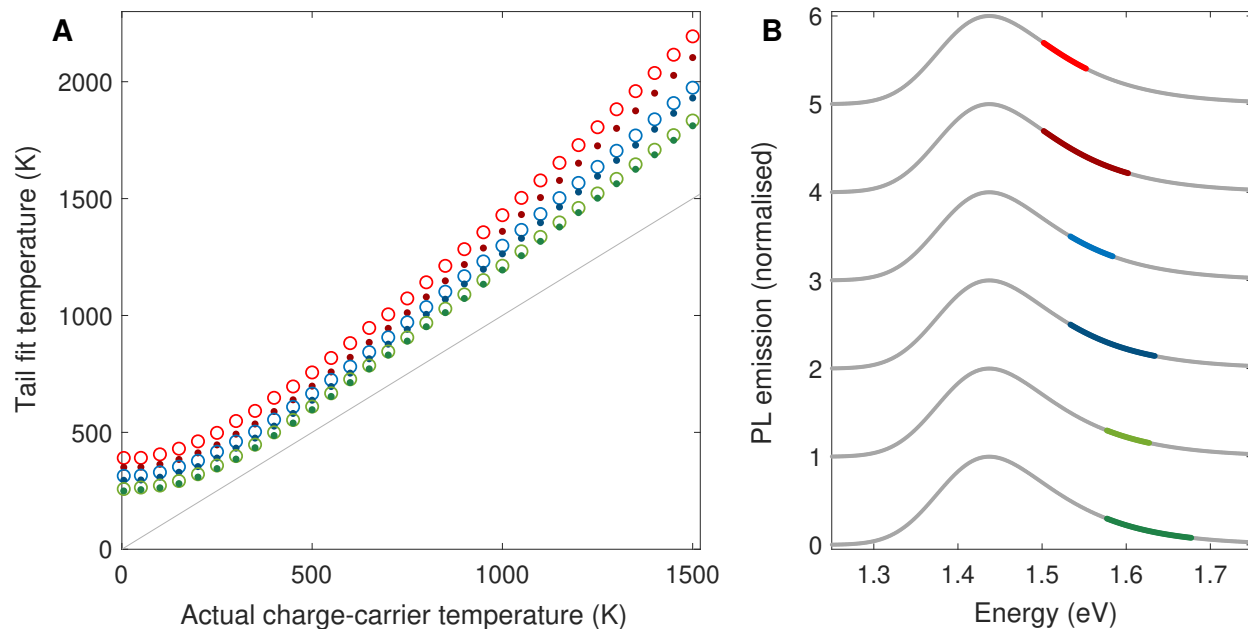


Figure S8: Charge-carrier temperatures (A) extracted from exponential tail fits to selected tail regions of a PL spectrum modelled using Equations S1 - S3 with $E_g = 1.38$ eV and $\sigma = 43.4$ meV (B) demonstrating the impact of choice of tail region on the temperature extracted from exponential tail fits. A) Charge-carrier temperatures determined by exponential fits to a selected tail region of modelled PL spectra as illustrated in (B). Each temperature series corresponds to a different choice of tail, beginning at 70%, 50% or 30% of the peak emission amplitude with a range of either 50 meV (open circle markers) or 100 meV (point markers). The grey line is a guide to the eye indicating equality between actual input temperature and tail fit temperature. B) The different selections of tail region used for exponential fits, illustrated for the modelled PL spectrum with actual input temperature 750 K. Grey point markers are used for the modelled spectrum, with selected tail regions plotted in the same color as the corresponding temperature series in (A). For clarity, vertical offsets have been added to show each tail selection on a separate copy of the spectrum.

4.4 Impact of accounting for the joint density of states

Our model improves upon the frequently used exponential fit for describing hot charge-carrier PL by incorporating both the Boltzmann distribution and a factor for the joint density of states for electronic interband transitions in the underlying PL profile (Equation S2) and convolving this profile with Equation S3 to capture broadening. The impact of spectral broadening on fitted carrier temperatures is described in section 4.3 and becomes particularly significant for lower charge-carrier temperatures. Accounting for the contribution of the joint density of states to carrier distribution and the probability of radiative recombination at a given energy becomes more important for higher charge-carrier temperatures, as we describe here.

Figure S9A shows PL spectra modelled with Equations S1 - S3 using $E_g = 1.38$ eV and $\sigma = 43.4$ meV for a range of T_c values in the 5 to 1500 K range, with selected high energy tail regions marked in grey. Charge carrier temperatures extracted using an exponential fit to the selected tail region for a full set of similarly modelled spectra over this T_c range are plotted in Figure S9B using \times markers. The exponential tail fits can be seen from this to overestimate charge-carrier temperature for all spectra across the range, with values diverging as the actual input temperature increases. To determine how much of the overestimation is due to the assumption of an energy-independent (constant) density of states when fitting with an exponential, tail fit temperatures are also extracted by fitting with Equation S2 which accounts for a square-root density of states above E_g (the expected result for direct interband transitions in a semiconductor with parabolic bands) while neglecting spectral broadening. The tail fit temperatures using Equation S2, plotted in Figure S9B using $+$ markers, level out to a slightly lower value at the low temperature end of the range than the exponential tail fit temperatures, and show only a small overestimation above around 400 K with no divergence as charge-carrier temperature increases. This indicates that the divergence between fitted and actual input values of T_c at high temperature when a simple exponential model is used is entirely due to the incorrect assumption of a constant joint density of states, with only a small residual impact of spectral broadening at high charge-carrier temperatures.

To confirm this, we use the same E_g value and T_c range for the modelled spectra in Figure S9A

to model emission profiles with no broadening using Equation S2 only (shown in Figure S9C) and use exponential tail fits to these broadening-free data to extract charge-carrier temperatures as plotted in Figure S9D. The exponential tail fit temperatures for an emission profile without any broadening show no low-temperature plateau, and a consistent divergence from the actual input temperatures as T_c increases. It is clear that the overestimation by exponential fits at high charge-carrier temperatures is mostly unrelated to broadening, and results from neglecting the realistic density of states. Figure 1 in the main text offers a further illustration, showing the results of fits with Equation S2 to spectra with $\sigma = 43.4$ meV or $\sigma = 5$ meV. At high charge-carrier temperatures the fitted values for both higher and lower broadening are close to the actual input value, whereas at low charge-carrier temperatures there is substantial overestimation in the higher broadening case only. The relative error in fitted temperatures for each case, plotted in Figure S10, also makes this point clear: accounting for energy-dependent density of states gives more accurate fitted temperature values as charge-carrier temperature increases.

The overestimation of charge-carrier temperature from exponential tail fits which increases for higher temperatures is explained by comparing the more accurate density of states for direct transitions between parabolic bands to the simplified constant JDOS, flat band model. For energies further above the bandgap, the difference between constant and square-root joint densities of states is greater. Higher charge-carrier temperatures correspond to the energetic distribution of charge-carriers extending to higher energies, so that for hotter populations the choice of model for density of states has a greater impact on how close the value of T_c extracted from an exponential fit is to the actual charge-carrier temperature. This makes accounting for the density of states particularly important to accurately capture charge-carrier cooling shortly after excitation or at high excitation densities, when the charge-carrier population remains elevated for an extended period.

Both the joint density of states and the presence of spectral broadening, if ignored in fitting measured spectra for carrier temperature, lead to overestimations of the carrier temperature. The magnitude of these overestimates is quantified in Figure S10, which shows relative error in fitted temperatures assuming either constant or square-root density of states, as well as for varying σ val-

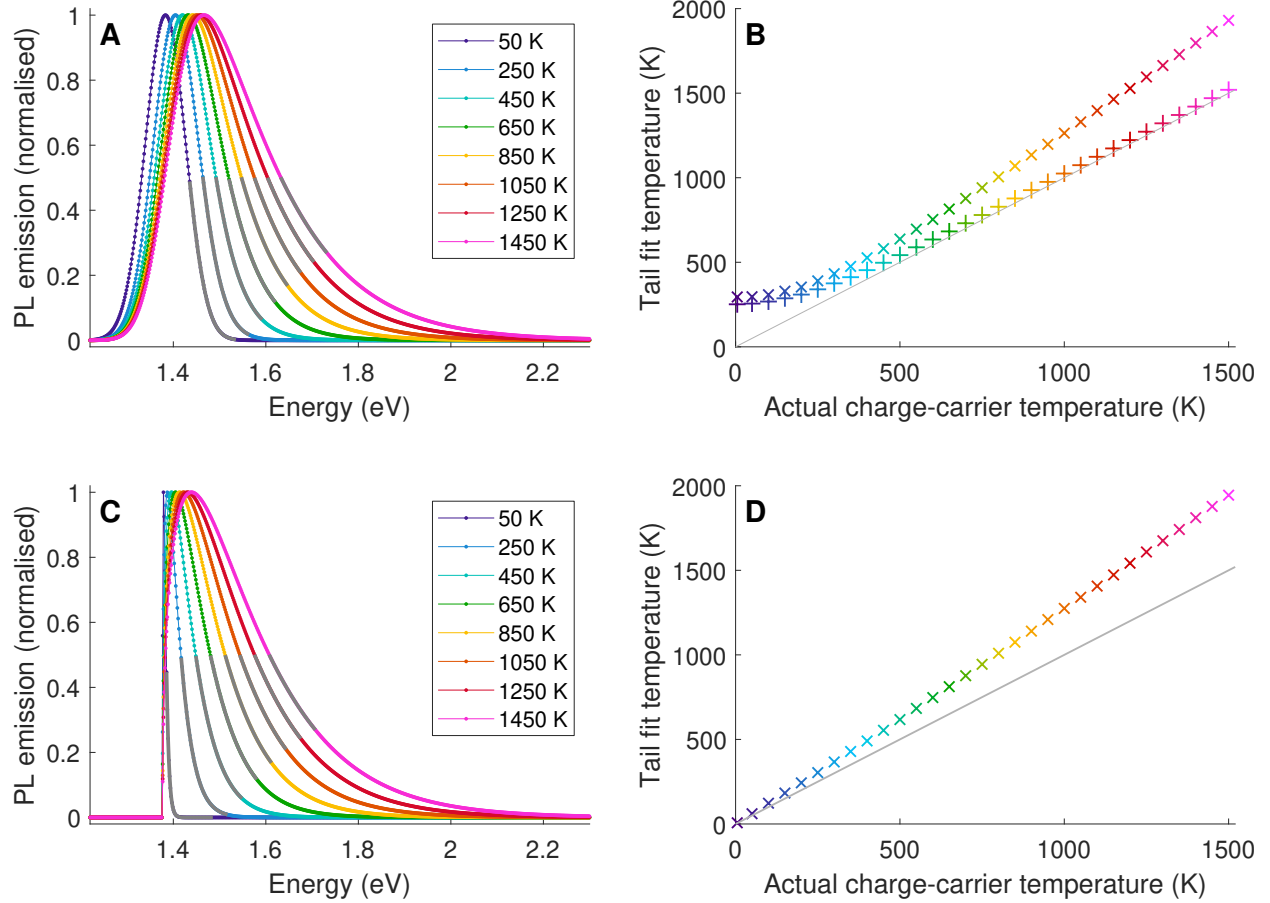


Figure S9: Impact of assuming a constant joint density of states for interband transitions on charge-carrier temperatures (B, D) extracted from fitting to the high energy tail of PL spectra modelled with (A) or without (C) broadening. Note that the realistic broadening case represented in (A, B) is the same as shown in Figure 1 of the main text, whereas in (C, D) no broadening whatsoever is included, a step further than the low broadening case in the main text. A) Representative selection of broadened PL spectra for T_c values between 5 - 1500 K as in the legend, modelled with Equations S1 - S3 using $E_g = 1.38$ eV and $\sigma = 43.4$ meV. Selected tail regions 0.1 eV in length starting from 50% of the peak emission amplitude are shown by grey lines overlaid on the spectra. B) Charge-carrier temperatures determined from fits to the tail regions as shown in (A) for the full set of modelled spectra from 5 - 1500 K. Charge-carrier temperatures extracted using an exponential fit which assumes a constant density of states are shown by \times markers, those extracted using Equation S2 which assumes a square-root joint density of states for energies above the band gap are shown by $+$ markers, illustrating the improvement in fits when the realistic density of states is accounted for. The marker color scheme matches that used for spectra in (A). The grey line is a guide to the eye indicating equality between actual input temperature and tail fit temperature. C) Representative selection of PL emission profiles without any broadening for T_c values between 5 - 1500 K as in the legend, modelled with Equation S2 using $E_g = 1.38$ eV. Selected tail regions 0.1 eV in length starting from 50% of the peak emission amplitude are shown by grey lines overlaid on the spectra. D) Charge-carrier temperatures determined from exponential fits to the tail regions as shown in (C), to illustrate the overestimation that remains by assuming a constant density of states when there is no broadening. The marker color scheme matches that used for spectra in (C). The grey line is a guide to the eye indicating equality between actual input temperature and tail fit temperature.

ues. As is apparent in the figure, overestimates are not constant for ranges of carrier temperatures likely to be encountered by experiment, and so failure to properly account for the various contributions to line shape is also likely to lead to incorrect estimates of cooling time. We avoid these problems through use of the full line shape model given by Equations S1 - S3, with the process of temperature fitting carried out as described in section 4.5

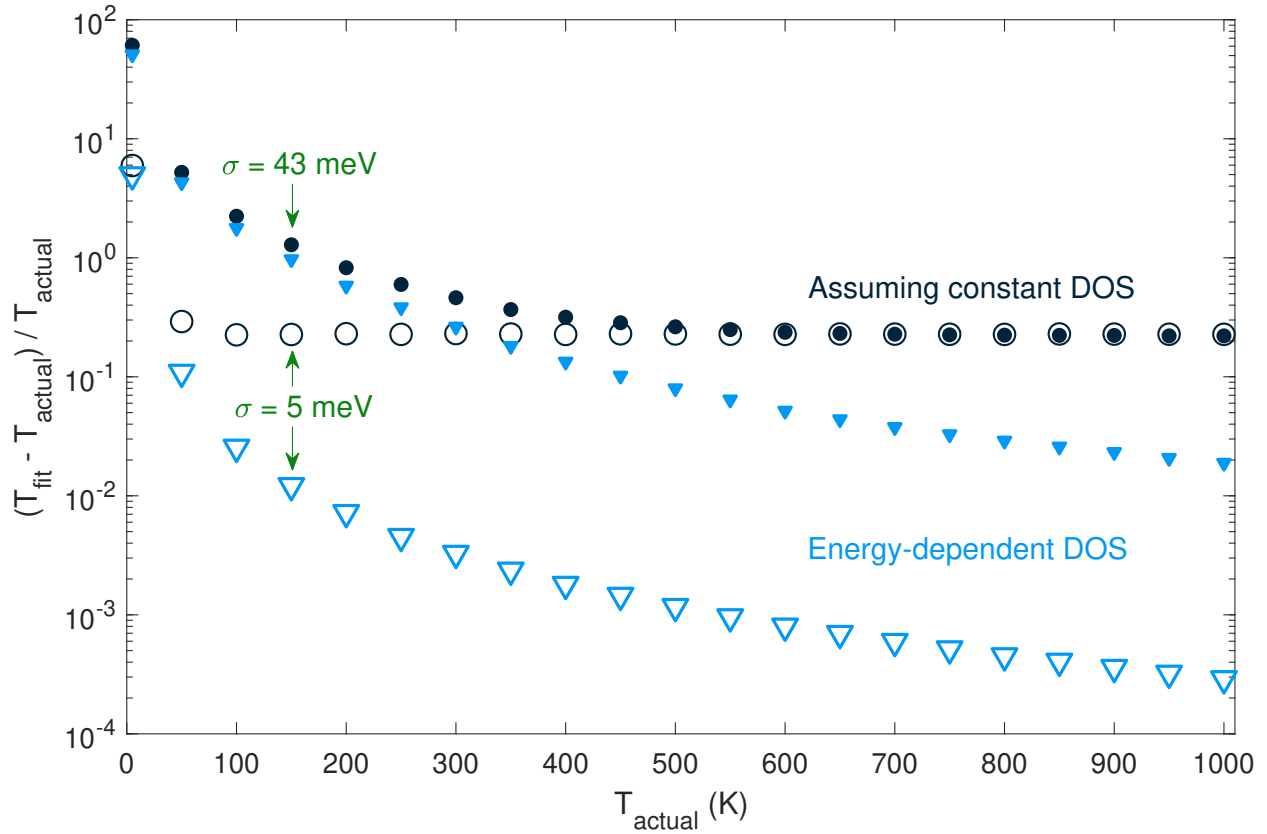


Figure S10: Relative error in carrier temperature as determined by fitting to a selected high energy tail region of the simulated PL spectrum. The temperatures T_{actual} are used as inputs in Equations S1 - S3 to model PL emission spectra, with $E_g = 1.38$ eV and σ value either 43.4 meV (point and filled triangle markers) or 5 meV (\circ and ∇ markers) as indicated. Fitted temperatures T_{fit} are then determined by fitting the high-energy side of the spectrum between 50% and 5% of maximum emission intensity with either an exponential (the Boltzmann only case assuming a constant density of states, shown by point and \circ markers) or Equation S2 (the Boltzmann & energy-dependent DOS for parabolic bands, shown by filled triangle and ∇ markers). The fit temperatures and marker color scheme used here correspond to Figure 1C in the main text.

4.5 Fitting procedure and results

Measured spectra are fitted with the model given by Equations S1 - S3 (expressed in the main text as Equation 1). This model is computed using Fourier transforms according to Equation S6 which holds for any pair of functions A and B .

$$A \otimes B = \mathcal{F}^{-1}[\mathcal{F}(A) \times \mathcal{F}(B)] \quad (\text{S6})$$

This approach has the advantage that the Gaussian which serves as the broadening function $f(E)$ has a Gaussian as its own Fourier transform, simplifying the process computationally. There are four parameters in our model to describe the spectrum, each of which can be either free or set to a known value: carrier temperature T_c , bandgap E_g , broadening parameter σ , and a scaling factor A for the proportionality in Equation S2 which accounts for the intensity of the peak as measured. Of these parameters, A is expected to vary with delay time as the population of carriers and correspondingly the intensity of the photoluminescence decay, and is therefore never fixed. The bandgap, by contrast, is a property of the sample which should be unchanged between measurements, and similarly the effects leading to broadening of the spectrum are not expected to vary widely.

Therefore, we determine characteristic values of E_g and σ for our FASnI₃ samples which are kept fixed in fitting all spectra to determine carrier temperature at different times after excitation. This is done separately for the two excitation powers we use here, since there is a small power-dependent peak shift observed for our samples separate from the influence of carrier temperature on line shape. As Figure S11 illustrates, a slight blue shift with increasing excitation power is consistently seen in both time-integrated measurements, where transient hot populations would have little influence on line shape, and in time-resolved spectra at a range of delay times. Measurements across a wider range of excitation fluences, shown in Figure S11A, confirm this to be a general trend beyond the two excitation fluences we focus on in this study, perhaps due to state filling as excitation density increases with fluence. Simple band filling within the square root density

of states is expected to have little effect at the charge-carrier densities generated here, which lie below the onset threshold for Burstein-Moss shifts determined previously,^{55–58} whereas filling of disordered energetic states can still occur at lower densities. If this excitation power effect were not accounted for, and a single set of parameter values was used for temperature fitting in all cases, there would be a tendency to overestimate carrier temperatures for the high excitation power spectra. Further, comparing figures S15 and S16 illustrates that the fitted spectra for the high fluence condition are better matched to the data when using the global parameter values determined from high fluence spectra than if global parameter values determined from low fluence spectra are used.

We note that the observed slight change in peak position with excitation fluence, and the resulting apparent change in bandgap, is consistent with state filling in the context of energetic disorder, which may also contribute to some red shift in the peak position as charge-carrier density decreases over time after excitation. Allowing the value of E_g to vary freely over time after excitation offers one route to accounting for these effects, but since there is a larger apparent red shift in peak position with decreasing T_c when E_g is held constant (illustrated in Figures S6A and S9A) we judge that fitting with variable E_g value risks overlooking real cooling dynamics, especially at early times. Moreover, comparing spectra measured at different delay times after excitation (Figure S11B) indicates that the small shift in peak position with excitation fluence is preserved over time, and so can be considered independently from the small time-dependent red shift and reduction in high energy emission. Therefore, we are able to keep charge-carrier temperature determination simple with T_c the only free parameter in fitting, and use different fixed E_g values to account for fluence dependent effects and avoid overestimating charge-carrier temperature in the higher fluence condition.

The procedure used to determine the characteristic values of E_g and σ involves taking spectra measured at 0.6 to 0.7 ns after photoexcitation, a sufficiently late time that no further cooling is seen, and setting T_c to 300 K as the expected final temperature for carriers equilibrated with the lattice. Global fits are then conducted for E_g and σ over the selected set of spectra, as illustrated in Figure S12 for the low excitation power case, and Figure S13 for high excitation power. The resulting parameter values, shown in Table S2 below, completely define the form of the broadening

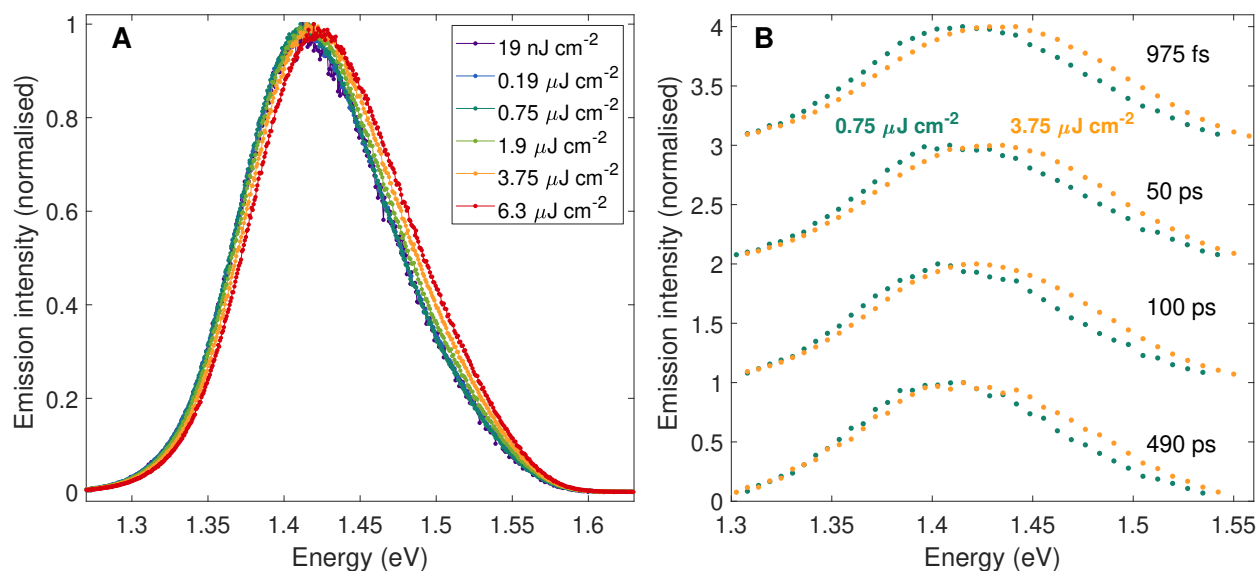


Figure S11: Photoluminescence spectra of FASnI₃ thin films on quartz under varying excitation fluence. A) Time integrated spectra measured for excitation powers ranging from 19 nJ cm⁻² to 6.3 μJ cm⁻², with acquisition times adjusted to maximise signal to noise for each excitation condition. Each spectrum is normalised to its own maximum signal for ease in comparing peak positions. B) Time-resolved spectra measured by PL upconversion spectroscopy (975 fs and 50 ps) or TCSPC (100 ps and 490 ps) for 0.75 μJ cm⁻² and 3.75 μJ cm⁻² excitation power as indicated, shown in green and gold respectively to match the color scale in (A). All points at or above 10% of maximum are shown for each spectrum, capturing the same range used to fit temperatures. Spectra are normalised to their maximum intensity, and vertical offsets have been added for clarity.

function $f(E)$ for this system.

Table S2: Characteristic values of the parameters E_g and σ used in equations S1 - S3 as determined by global fits over late time photoluminescence spectra.

	$0.75 \mu\text{J cm}^{-2}$ excitation fluence	$3.75 \mu\text{J cm}^{-2}$ excitation fluence
E_g [eV]	1.3767	1.3850
σ [eV]	0.0434	0.0483

We then determine carrier temperatures by fitting the measured spectra with the parameters E_g and σ fixed to the values determined from the late-time fits just described, allowing temperature and scaling factor A to vary for each individual spectrum. Representative examples of the fitted spectra in comparison to measured data with low excitation power are shown in Figure S14, and similarly with high excitation power in Figure S15.

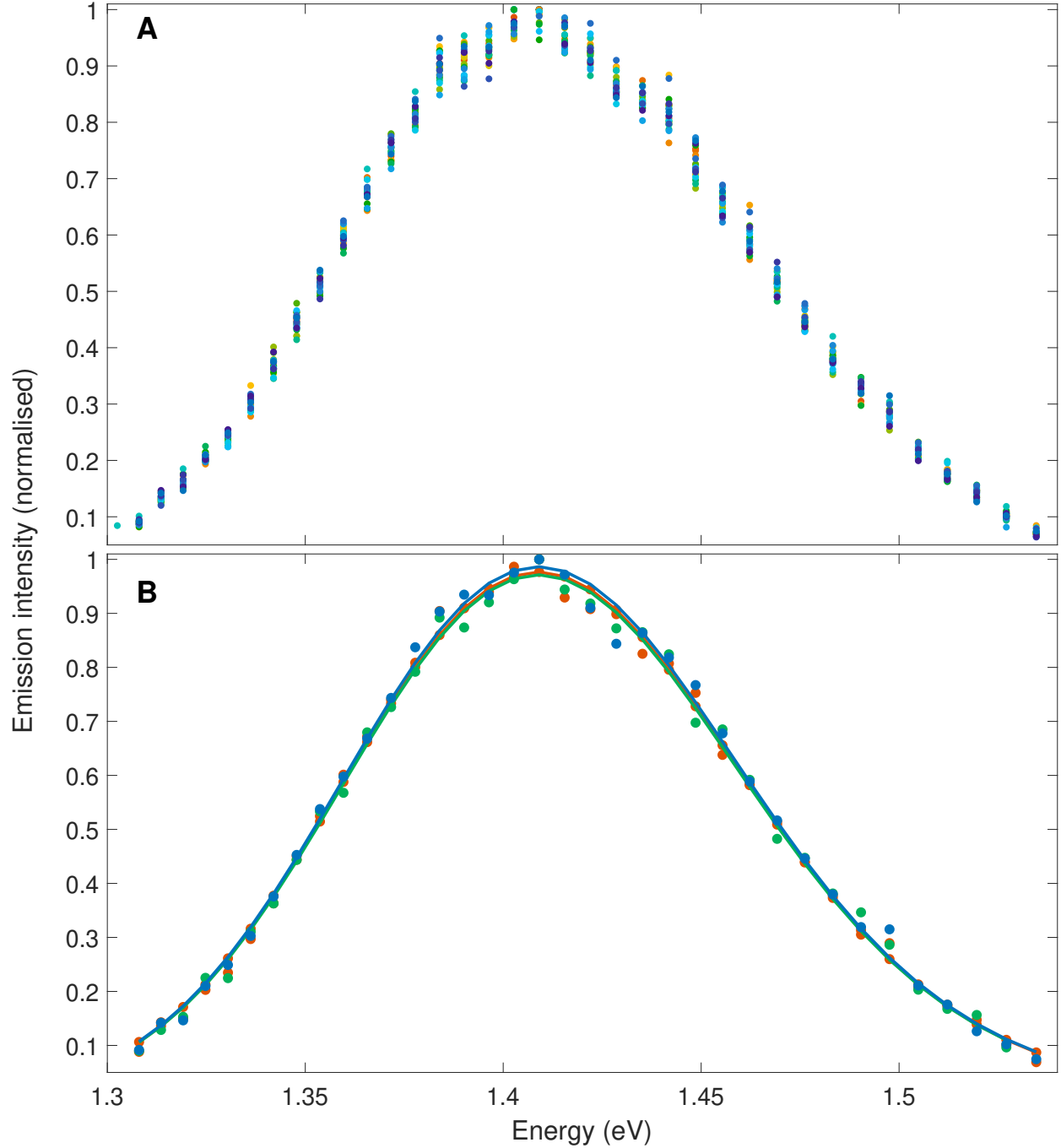


Figure S12: Time-resolved photoluminescence spectra of FASnI₃ films on quartz measured by TCSPC with $0.75 \mu\text{J cm}^{-2}$ excitation fluence at late delay times. Global fits to these spectra using Equations S1 – S3 with charge-carrier temperature set to 300 K are used to determine characteristic values of E_g and σ for PL emission spectra measured with low excitation fluence, as recorded in Table S2. A) All measured PL spectra from 0.6 - 0.7 ns, illustrating noise levels and variation between spectra within the time interval selected for global fitting. Marker colors range from red to blue as delay time increases. B) Measured (point markers) and fitted (solid lines) spectra at 0.6, 0.65 and 0.7 ns delay, with marker colors the same as for these delay times in (A). The fitted spectra are given by Equations S1 - S3 with charge-carrier temperature set to 300 K, and globally fitted parameter values $E_g = 1.3767 \text{ eV}$ and $\sigma = 43.4 \text{ meV}$.

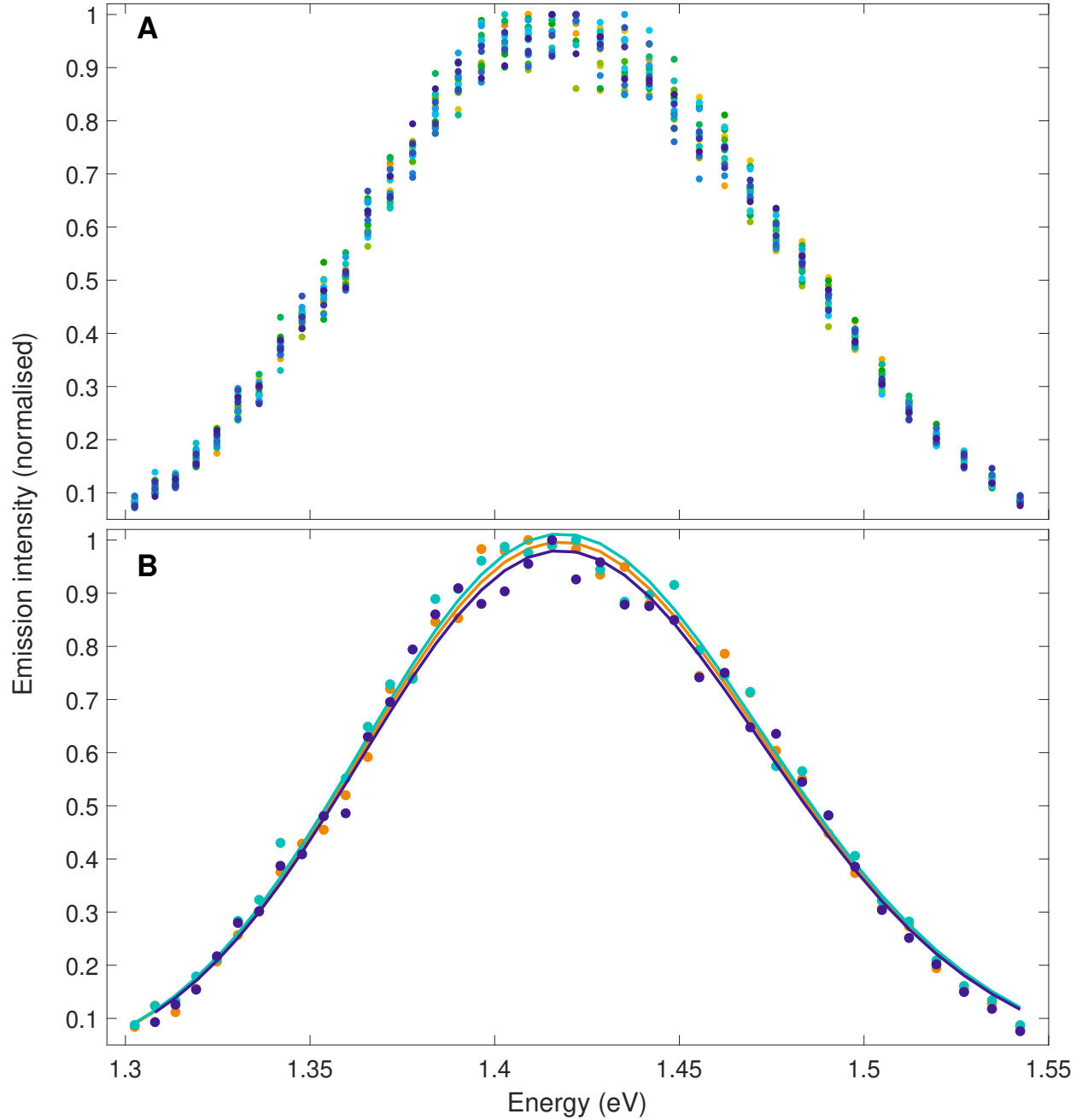


Figure S13: Time-resolved photoluminescence spectra of FASnI₃ films on quartz measured by TCSPC with $3.75 \mu\text{J cm}^{-2}$ excitation fluence at late delay times. Global fits to these spectra using equations S1 - S3 with charge-carrier temperature set to 300 K are used to determine characteristic values of E_g and σ for PL emission spectra measured with low excitation fluence, as recorded in Table S2. A) All measured PL spectra from 0.6 - 0.7 ns, illustrating noise levels and variation between spectra within the time interval selected for global fitting. Marker colors range from red to blue as delay time increases. B) Measured (point markers) and fitted (solid lines) spectra at 0.6, 0.65 and 0.7 ns delay, with marker colors the same as for these delay times in (A). The fitted spectra are given by Equations S1 - S3 with charge-carrier temperature set to 300 K, and globally fitted parameter values $E_g = 1.3850 \text{ eV}$ and $\sigma = 48.3 \text{ meV}$.

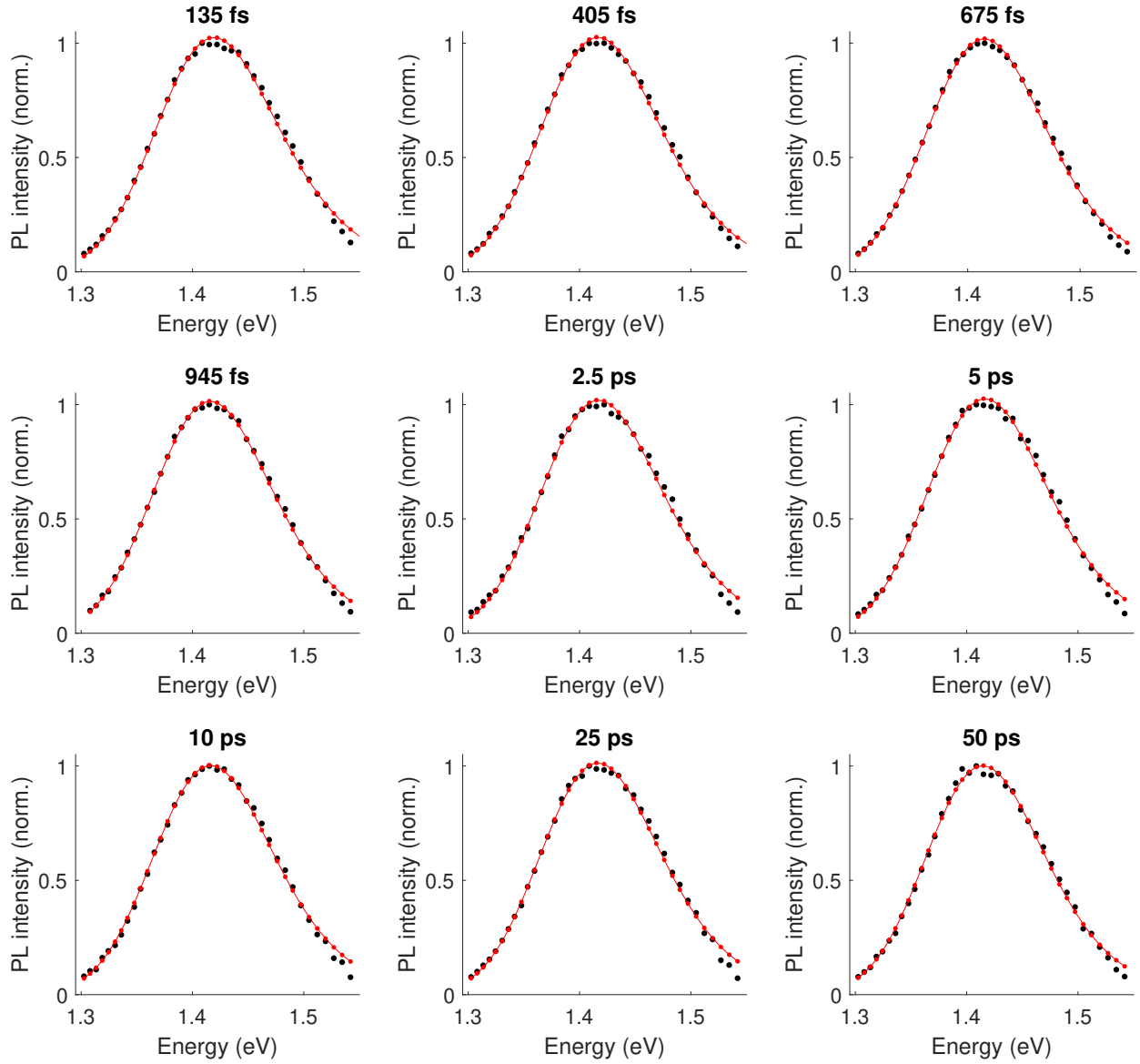


Figure S14: PL spectra of a FASnI₃ film on quartz, excited at 730 nm with $0.75 \mu\text{J cm}^{-2}$ excitation fluence, with fits used to extract charge-carrier temperature. Black point markers are data measured by PL upconversion spectroscopy, and averaged at the delay times indicated where multiple spectra at the same time (to within system resolution) had been acquired. Red solid lines are fits for T_c using Equations S1 - S3 as a full line shape model with $E_g = 1.3767$ eV and $\sigma = 43.4$ meV as fixed parameters. The charge-carrier temperatures obtained from these fits are used in the cooling curve shown in Figure 2C in the main text.

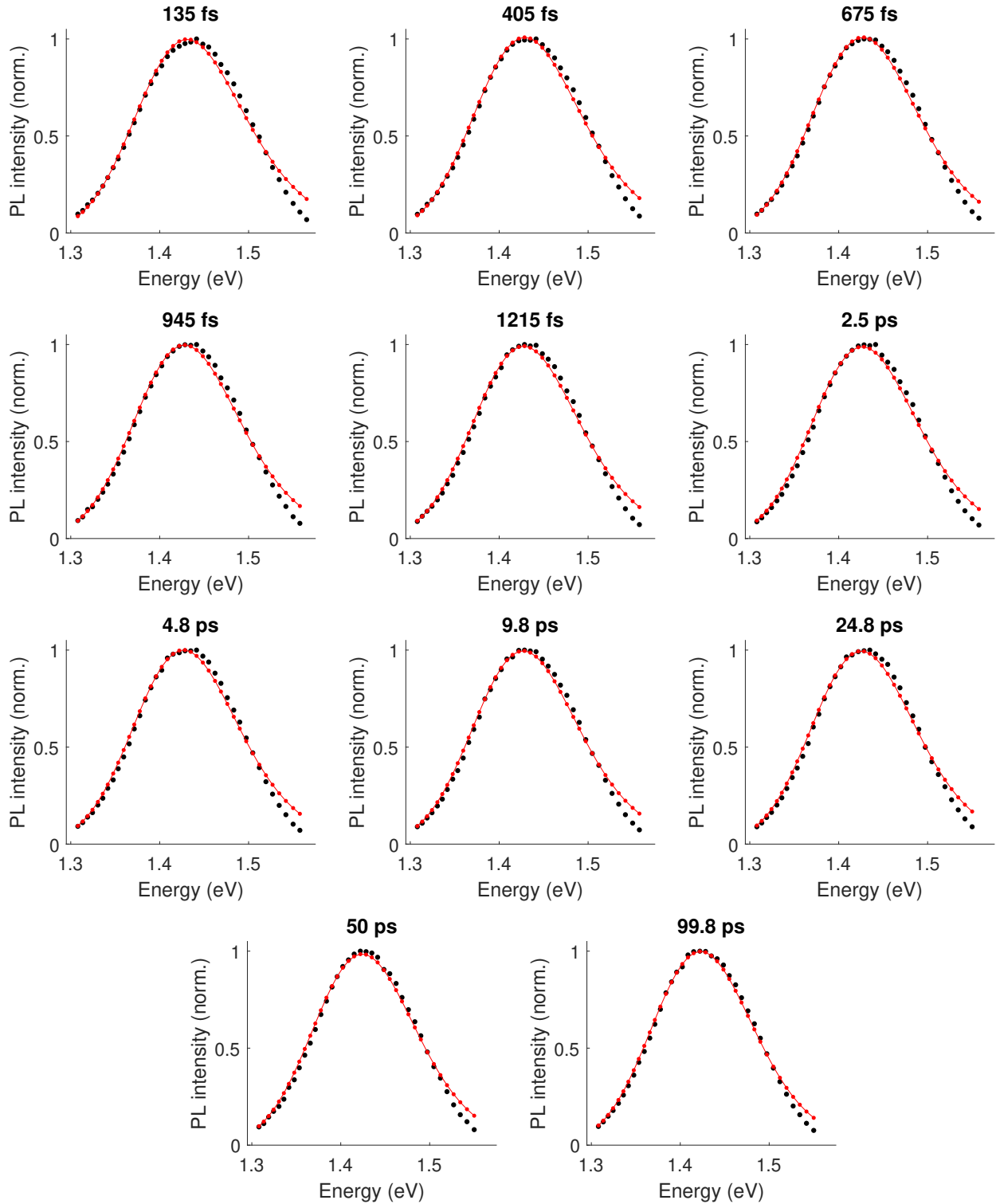


Figure S15: PL spectra of a FASnI₃ film on quartz, excited at 730 nm with $3.75 \mu\text{J cm}^{-2}$ excitation fluence, with fits used to extract charge-carrier temperature. Black point markers are data measured by PL upconversion spectroscopy, and averaged at the delay times indicated where multiple spectra at the same time (to within system resolution) had been acquired. Red solid lines are fits for T_c using Equations S1 - S3 as a full line shape model with $E_g = 1.3850 \text{ eV}$ and $\sigma = 48.3 \text{ meV}$ as fixed parameters. The charge-carrier temperatures obtained from these fits are used in the cooling curve shown in Figure 2B in the main text.

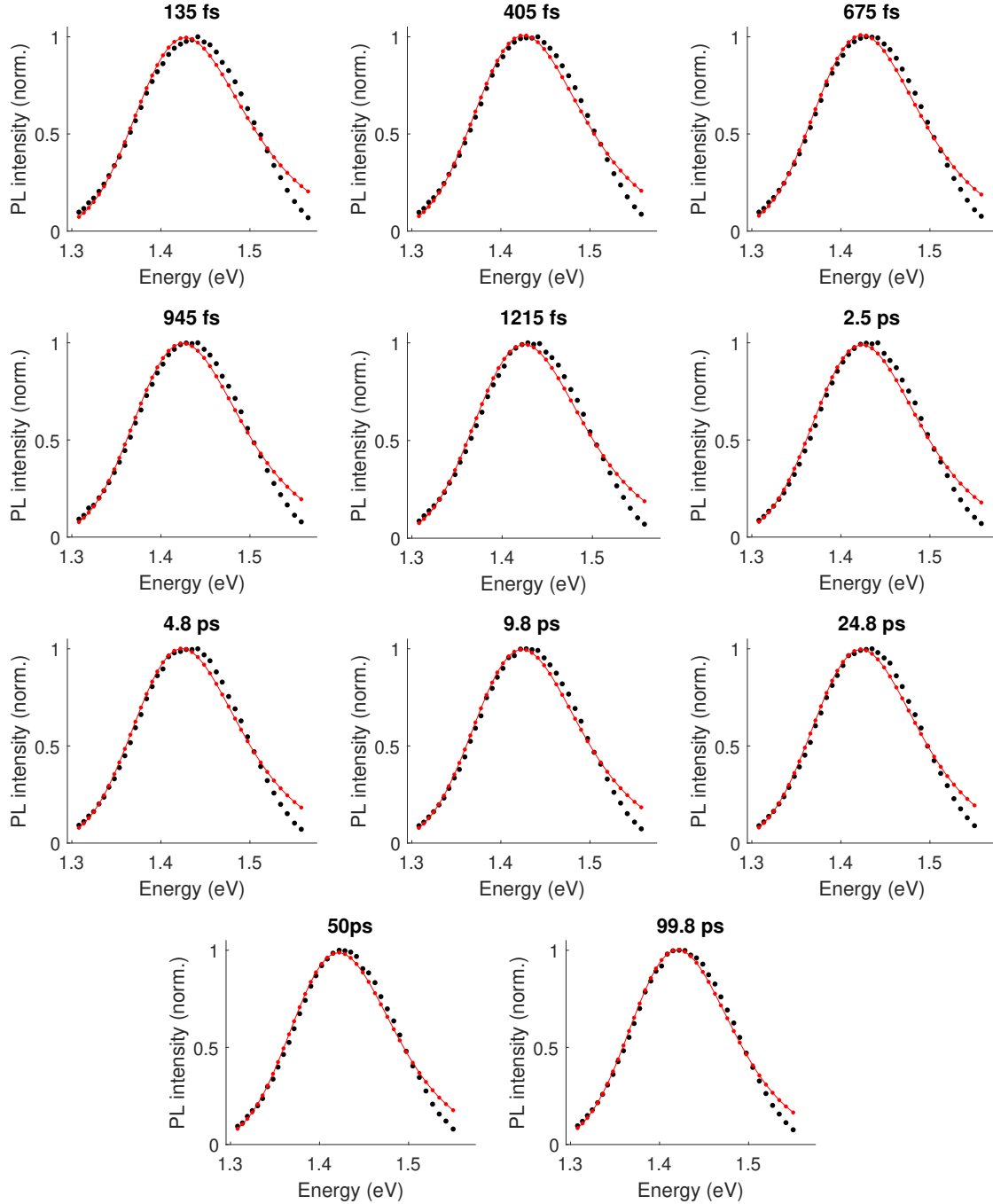


Figure S16: PL spectra of a FASnI₃ film on quartz, excited at 730 nm with $3.75 \mu\text{J cm}^{-2}$ excitation fluence, with fits used to extract charge-carrier temperature. Black point markers are data measured by PL upconversion spectroscopy, and averaged at the delay times indicated where multiple spectra at the same time (to within system resolution) had been acquired. Red solid lines are fits for T_c using Equations S1 - S3 as a full line shape model with $E_g = 1.3767 \text{ eV}$ and $\sigma = 43.4 \text{ meV}$ as fixed parameters. These are the parameter values determined for late-time spectra with $0.75 \mu\text{J cm}^{-2}$ excitation fluence, which result in fitted spectra which are less close to the measured data at high fluence than the fits shown in Figure S15 where the E_g and σ values specific to high excitation fluence are used.

5 Additional PL decay curves

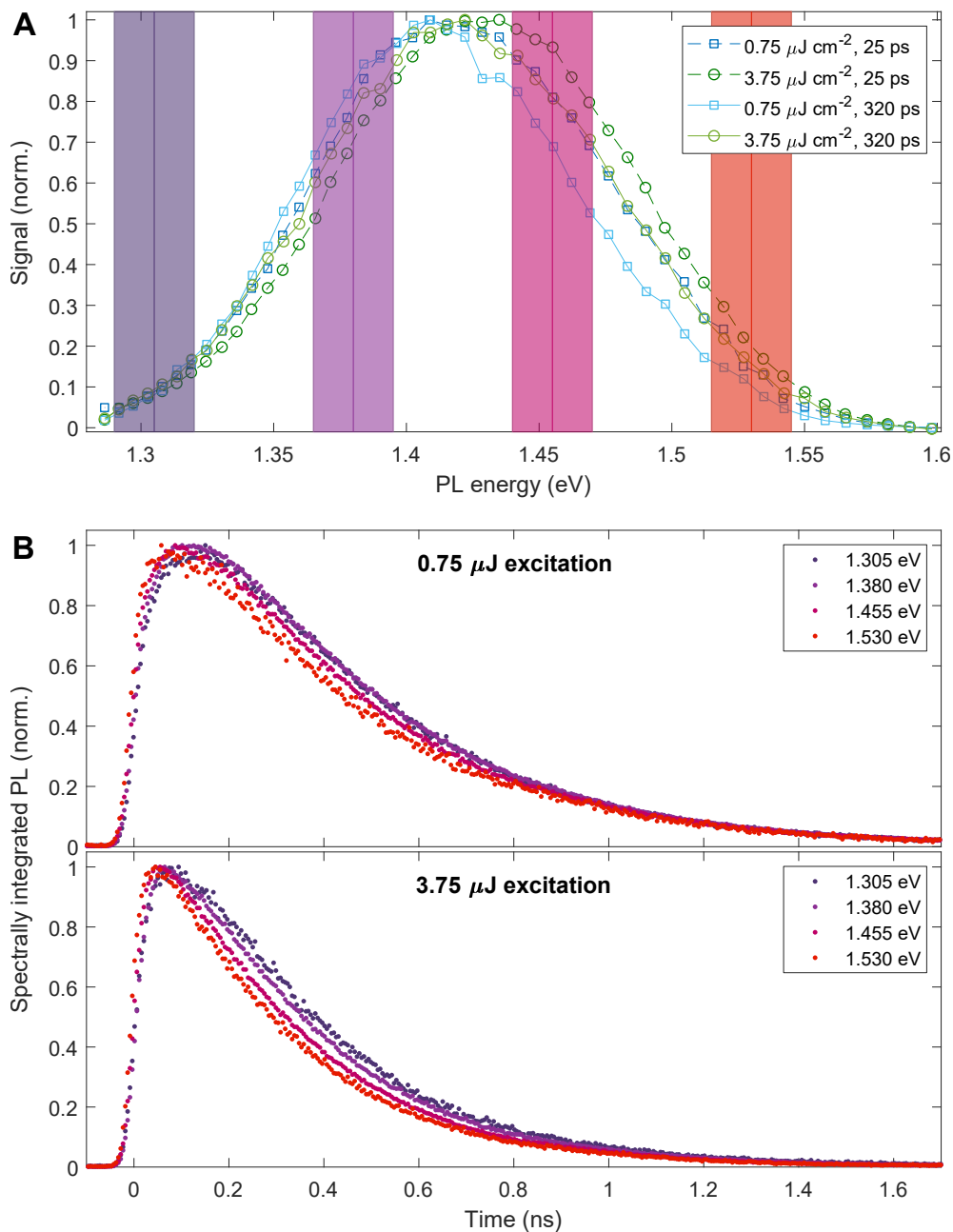


Figure S17: Photoluminescence decay transients integrated over selected spectral regions of the emission of a FASnI₃ film on quartz. A) PL spectra, showing early and late delay times for both excitation fluences, with selected 30 meV energy ranges for integration highlighted. Each selected energy range is identified by the center energy, marked by a darker solid line within the highlighted bar. B) Integrated decay transients for low and high excitation fluences as marked, using the same color scheme for energy as in (A).

6 Polarization anisotropy measurements

Upconversion spectroscopy is intrinsically polarization selective, with sum frequency generation occurring only for the component of photoluminescence which matches the polarization of the gate beam. By changing the pump polarization used to excite the sample, photoluminescence can therefore be detected with polarization either parallel or perpendicular to the original excitation polarization. PL polarization anisotropy is then calculated from the intensities in each configuration using Equation S7:

$$r = \frac{I_{\parallel} - I_{\perp}}{I_{\parallel} + 2I_{\perp}} \quad (\text{S7})$$

where I_{\parallel} (I_{\perp}) is the intensity of light with polarization parallel (perpendicular) to the excitation polarization.

The key features of our setup for these measurements are illustrated in Figure S18, with the half waveplate in the pump beam being used to tune excitation power to the same value for both polarizations. Following each change between 0° and 90° polarization, small adjustments to alignment are also made to return to optimal overlap of the two beams in the crystal, giving maximum upconversion signal. This step is necessary due to the slight change in direction of the transmitted beam when waveplate and polarizer angles are changed.

To account for variation in signal intensity resulting from remaining experimental error, we conduct a series of measurements at a single delay time (3 ps, where the decay transient is not rapidly changing) and PL energy (1.42 eV, around the peak of the spectrum), repeatedly switching between polarizations and working with three different sample spots. For each consecutive pair of measured signal values, some of which begin with the parallel polarization and some with perpendicular, the PL anisotropy is then calculated. The results are shown in Figure S19, along with the mean value of 0.0146 obtained for the full set of ten values. The standard deviation for the set is 0.0441, as indicated by the error bars shown on the mean value.

Rearranging Equation S7 we determine the ratio $\frac{I_{\perp}}{I_{\parallel}} = 0.9575$. This value is then used to scale spectra measured for 90° polarization against the corresponding spectra for 0° polarization at the

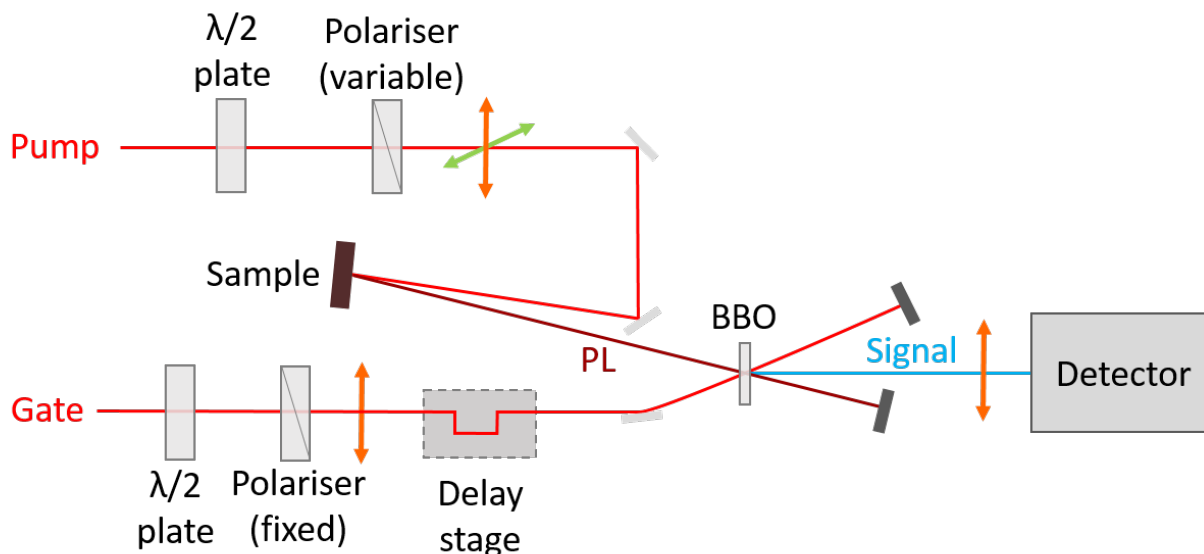


Figure S18: Simplified schematic of the experimental setup for polarization selective PL upconversion spectroscopy measurements. Arrows indicate the polarization direction of each beam, orange for vertical and green for horizontal, both at right angles to the beam path. The unlabelled rectangles represent beam dumps for the transmitted pump and gate beams after the BBO crystal.

energy used for the checks just described, which allows anisotropy values to be calculated across the full spectral range. Similarly, the 90° transient delay data covering the earliest time range are scaled against the corresponding 0° data at 3 ps, after which the longer-time range data at each polarization are stitched to the earlier scans to yield the composite delay profiles shown in Figure 3 of the main text from which time-dependent anisotropies are calculated. This process ensures that differences in intensity which may result from imperfect re-alignment after changing polarization or from small variations in the sample are corrected for.

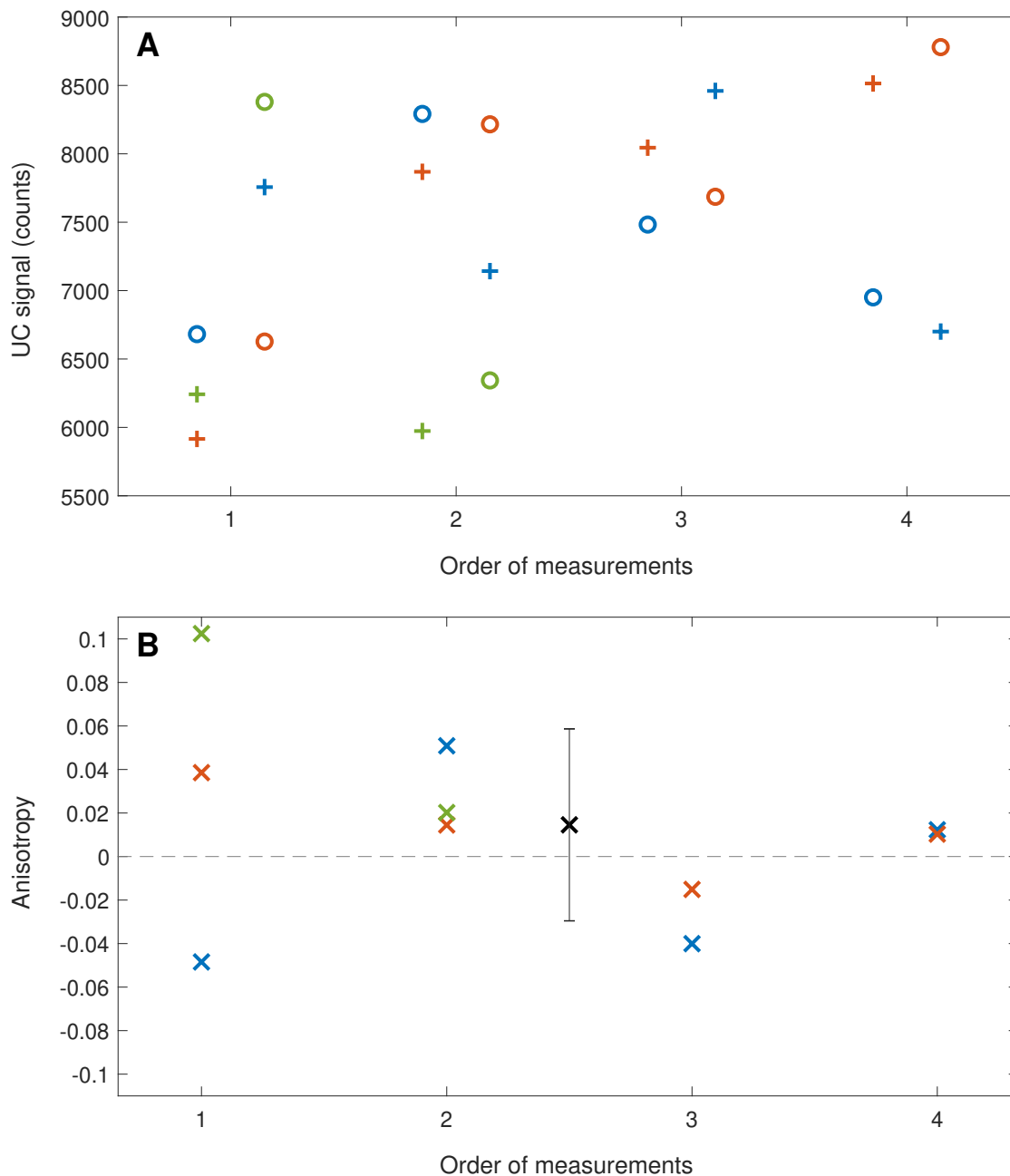


Figure S19: PL polarization anisotropy measurements with repeated polarization switching, measuring 1.42 eV photoluminescence at a delay time of 3 ps, exciting the FASnI_3 sample with 730 nm pump beam at a fluence of $0.75 \mu\text{J cm}^{-2}$ for two polarizations, one parallel (0°) and one perpendicular (90°) to the detected PL polarization. A) Measured signal values after optimising signal for each polarization. Marker colors correspond to the three different sample spots used, with + markers for 90° polarization, ○ markers for 0° polarization. For each sample spot series, values are plotted in the temporal order in which they were measured. B) Anisotropy values calculated from the measured intensities shown in (A), following the same color scheme to distinguish sample spots. The mean anisotropy value across all ten points is also shown, in black, with the error bar calculated as the standard deviation.

References

- (1) Chang, M. H.; Hoeben, F. J.; Jonkheijm, P.; Schenning, A. P.; Meijer, E. W.; Silva, C.; Herz, L. M. Influence of Mesoscopic Ordering on the Photoexcitation Transfer Dynamics in Supramolecular Assemblies of oligo-p-Phenylenevinylene. *Chem. Phys. Lett.* **2006**, *418*, 196–201.
- (2) Chang, M. H.; Hoffmann, M.; Anderson, H. L.; Herz, L. M. Dynamics of Excited-State Conformational Relaxation and Electronic Delocalization in Conjugated Porphyrin Oligomers. *J. Am. Chem. Soc.* **2008**, *130*, 10171–10178.
- (3) Gong, J. Q.; Parkinson, P.; Kondratuk, D. V.; Gil-Ramírez, G.; Anderson, H. L.; Herz, L. M. Structure-Directed Exciton Dynamics in Templated Molecular Nanorings. *J. Phys. Chem. C* **2015**, *119*, 6414–6420.
- (4) Price, M. B.; Butkus, J.; Jellicoe, T. C.; Sadhanala, A.; Briane, A.; Halpert, J. E.; Broch, K.; Hodgkiss, J. M.; Friend, R. H.; Deschler, F. Hot-Carrier Cooling and Photoinduced Refractive Index Changes in Organic-Inorganic Lead Halide Perovskites. *Nat. Commun.* **2015**, *6*, 8420.
- (5) Yang, Y.; Ostrowski, D. P.; France, R. M.; Zhu, K.; van de Lagemaat, J.; Luther, J. M.; Beard, M. C. Observation of a Hot-Phonon Bottleneck in Lead-Iodide Perovskites. *Nat. Photonics* **2016**, *10*, 53–59.
- (6) Richter, J. M.; Branchi, F.; Valduga de Almeida Camargo, F.; Zhao, B.; Friend, R. H.; Cerullo, G.; Deschler, F. Ultrafast Carrier Thermalization in Lead Iodide Perovskite Probed with Two-Dimensional Electronic Spectroscopy. *Nat. Commun.* **2017**, *8*, 376.
- (7) Shen, Q.; Ripolles, T. S.; Even, J.; Ogomi, Y.; Nishinaka, K.; Izuishi, T.; Nakazawa, N.; Zhang, Y.; Ding, C.; Liu, F. et al. Slow Hot Carrier Cooling in Cesium Lead Iodide Perovskites. *Appl. Phys. Lett.* **2017**, *111*, 153903.
- (8) Li, M.; Bhaumik, S.; Goh, T. W.; Kumar, M. S.; Yantara, N.; Grätzel, M.; Mhaisalkar, S.; Mathews, N.; Sum, T. C. Slow Cooling and Highly Efficient Extraction of Hot Carriers in Colloidal Perovskite Nanocrystals. *Nat. Commun.* **2017**, *8*, 14350.

- (9) Shen, Q.; Ripolles, T. S.; Even, J.; Zhang, Y.; Ding, C.; Liu, F.; Izuishi, T.; Nakazawa, N.; Toyoda, T.; Ogomi, Y. et al. Ultrafast Selective Extraction of Hot Holes from Cesium Lead Iodide Perovskite Films. *J. Energy Chem.* **2018**, *27*, 1170–1174.
- (10) Nah, S.; Spokoyny, B. M.; Soe, C. M. M.; Stoumpos, C. C.; Kanatzidis, M. G.; Harel, E. Ultrafast Imaging of Carrier Cooling in Metal Halide Perovskite Thin Films. *Nano Lett.* **2018**, *18*, 1044–1048.
- (11) Chen, J.; Messing, M. E.; Zheng, K.; Pullerits, T.; Messing, M. E.; Zheng, K.; Pullerits, T. Cation-Dependent Hot Carrier Cooling in Halide Perovskite Nanocrystals. *J. Am. Chem. Soc.* **2019**, *141*, 3532–3540.
- (12) Papagiorgis, P.; Protesescu, L.; Kovalenko, M. V.; Othonos, A.; Itskos, G. Long-Lived Hot Carriers in Formamidinium Lead Iodide Nanocrystals. *J. Phys. Chem. C* **2017**, *121*, 12434–12440.
- (13) Yang, J.; Wen, X.; Xia, H.; Sheng, R.; Ma, Q.; Kim, J.; Tapping, P.; Harada, T.; Kee, T. T. W.; Huang, F. et al. Acoustic-Optical Phonon Up-Conversion and Hot-Phonon Bottleneck in Lead-Halide Perovskites. *Nat. Commun.* **2017**, *8*, 14120.
- (14) Verma, S. D.; Gu, Q.; Sadhanala, A.; Venugopalan, V.; Rao, A. Slow Carrier Cooling in Hybrid Pb–Sn Halide Perovskites. *ACS Energy Lett.* **2019**, *4*, 736–740.
- (15) Shah, J.; Leite, R. C. C. Radiative Recombination from Photoexcited Hot Carriers in GaAs. *Phys. Rev. Lett.* **1969**, *22*, 22–25.
- (16) Motisuke, P.; Argüello, C. A.; Leite, R. C. C. Hot Electron and Hot Phonon Contributions to Radiative Emission Spectra in CdS at High Excitation Intensities. *Solid State Commun.* **1975**, *16*, 763–765.
- (17) Shah, J.; Lin, C.; Leheny, R. F.; DiGiovanni, A. E. Pump Wavelength Dependence of Hot Electron Temperature in GaAs. *Solid State Commun.* **1976**, *18*, 487–489.
- (18) Ryan, J. F.; Taylor, R. A.; Turberfield, A. J.; Maciel, A.; Worlock, J. M.; Gossard, A. C.; Wiegmann, W. Time-Resolved Photoluminescence of Two-Dimensional Hot Carriers in GaAs-AlGaAs Heterostructures. *Phys. Rev. Lett.* **1984**, *53*, 1841–1844.

- (19) Xu, Z. Y.; Tang, C. L. Picosecond Relaxation of Hot Carriers in Highly Photoexcited Bulk GaAs and GaAs-AlGaAs Multiple Quantum Wells. *Appl. Phys. Lett.* **1984**, *44*, 692–694.
- (20) Shum, K.; Ho, P.; Alfano, R.; Welch, D.; Wicks, G.; Eastman, L. Dependence of Electron Temperature on Well Width in the $\text{Al}_{0.48}\text{In}_{0.52}\text{As}/\text{Ga}_{0.47}\text{In}_{0.53}\text{As}$ Single-Quantum Well. *IEEE J. Quantum Electron.* **1986**, *QE-22*, 1811–1815.
- (21) Leo, K.; Rühle, W. W. Influence of Carrier Lifetime on the Cooling of a Hot Electron-Hole Plasma in GaAs. *Solid State Commun.* **1987**, *62*, 659–662.
- (22) Andersson, T. G.; Chen, Z.-G.; Xu, Z.-Y.; Xu, J.-Z.; Ge, W.-K. Hot Carrier Photoluminescence from Strained $\text{In}_x\text{Ga}_{1-x}\text{As}/\text{GaAs}$ Single Quantum Wells. *J. Cryst. Growth* **1989**, *95*, 215–219.
- (23) Ge, W.; Xu, Z.; Li, Y.; Xu, Z.; Xu, J.; Zheng, B.; Zhuang, W. Hot Carrier Relaxation Processes and Nonequilibrium Phonon Effect in Multiple Quantum Well Structures. *J. Lumin.* **1990**, *46*, 137–145.
- (24) Mooradian, A.; Fan, H. Y. Recombination Emission in InSb. *Phys. Rev.* **1966**, *148*, 873–885.
- (25) Ulbrich, R. Energy Relaxation of Photoexcited Hot Electrons in GaAs. *Physical Review B* **1973**, *8*, 5719–5727.
- (26) Meneses, E. A.; Jannuzzi, N.; Ramos, J. G. P.; Luzzi, R.; Leite, R. C. C. Many-Body and Hot-Phonon Effects in the Radiative Emission Spectrum of CdS Under High Excitation Intensities. *Phys. Rev. B* **1975**, *11*, 2213.
- (27) Kash, K.; Shah, J. Carrier Energy Relaxation in $\text{In}_{0.53}\text{Ga}_{0.47}\text{As}$ Determined from Picosecond Luminescence Studies. *Appl. Phys. Lett.* **1984**, *45*, 401–403.
- (28) Collet, J. H.; Rühle, W. W.; Pugnet, M.; Leo, K.; Million, A. Electron-Hole Plasma Dynamics in CdTe in the Picosecond Regime. *Physical Review B* **1989**, *40*, 12296.
- (29) Collet, J. H.; Rühle, W. W.; Pugnet, M.; Leo, K.; Million, A. Electron-Hole Plasma Relaxation in CdTe. *J. Cryst. Growth* **1990**, *101*, 773–777.
- (30) Ryan, J. F. Time-Resolved Photoluminescence for Quantum Well Semiconductor Heterostructures. *Physica B+C* **1985**, *134*, 403–411.

- (31) Leo, K.; Rühle, W. W.; Ploog, K. Hot-Carrier Energy-Loss Rates in GaAs/Al_xGa_{1-x}As Quantum Wells. *Phys. Rev. B* **1988**, *38*, 1947–1957.
- (32) Leo, K.; Rühle, W. W.; Queisser, H. J.; Ploog, K. Reduced Dimensionality of Hot-Carrier Relaxation in GaAs Quantum Wells. *Phys. Rev. B* **1988**, *37*, 7121–7124.
- (33) Leo, K.; Rühle, W. W.; Ploog, K. Hot Carrier Thermalization in GaAs/AlAs Superlattices. *Solid-State Electron.* **1989**, *32*, 1863–1867.
- (34) Nozik, A. J.; Parsons, C. A.; Dunlavy, D. J.; Keyes, B. M.; Ahrenkiel, R. K. Dependence of Hot Carrier Luminescence on Barrier Thickness in GaAs/AlGaAs Superlattices and Multiple Quantum Wells. *Solid State Commun.* **1990**, *75*, 297–301.
- (35) Ploog, K.; Fischer, A.; Tapfer, L.; Feuerbacher, B. F. Narrow Luminescence Linewidth in GaAs Single Quantum Wells by Insertion of Thin AlAs Smoothing Layers. *J. Cryst. Growth* **1991**, *111*, 344–347.
- (36) Gotoh, H.; Akasaka, T.; Tawara, T.; Kobayashi, Y.; Makimoto, T.; Nakano, H. Efficient Observation of Narrow Isolated Photoluminescence Spectra from Spatially Localized Excitons in InGaN Quantum Wells. *Jpn. J. Appl. Phys., Part 2* **2005**, *44*, L1381–L1384.
- (37) Chen, K.; Barker, A. J.; Morgan, F. L. C.; Halpert, J. E.; Hodgkiss, J. M. Effect of Carrier Thermalization Dynamics on Light Emission and Amplification in Organometal Halide Perovskites. *J. Phys. Chem. Lett.* **2014**, *6*, 153–158.
- (38) Fang, H.-H.; Adjokatse, S.; Shao, S.; Even, J.; Loi, M. A. Long-Lived Hot-Carrier Light Emission and Large Blue Shift in Formamidinium Tin Triiodide Perovskites. *Nat. Commun.* **2018**, *9*, 243.
- (39) Schoenlein, R. W.; Lin, W. Z.; Ippen, E. P.; Fujimoto, J. G. Femtosecond Hot-Carrier Energy Relaxation in GaAs. *Appl. Phys. Lett.* **1987**, *51*, 1442–1444.
- (40) Rota, L.; Lugli, P.; Elsaesser, T.; Shah, J. Ultrafast Thermalization of Photoexcited Carriers in Polar Semiconductors. *Phys. Rev. B* **1993**, *47*, 4226.
- (41) Umari, P.; Mosconi, E.; De Angelis, F. Relativistic GW Calculations on CH₃NH₃PbI₃ and CH₃NH₃SnI₃ Perovskites for Solar Cell Applications. *Sci. Rep.* **2014**, *4*, 4467.

- (42) He, Y.; Galli, G. Perovskites for Solar Thermoelectric Applications: A First Principle Study of $\text{CH}_3\text{NH}_3\text{AI}_3$ (A= Pb and Sn). *Chemistry of Materials* **2014**, *26*, 5394–5400.
- (43) Davies, C. L.; Filip, M. R.; Patel, J. B.; Crothers, T. W.; Verdi, C.; Wright, A. D.; Milot, R. L.; Giustino, F.; Johnston, M. B.; Herz, L. M. Bimolecular Recombination in Methylammonium Lead Triiodide Perovskite is an Inverse Absorption Process. *Nat. Commun.* **2018**, *9*, 293.
- (44) Wehrenfennig, C.; Liu, M.; Snaith, H. J.; Johnston, M. B.; Herz, L. M. Homogeneous Emission Line Broadening in the Organo Lead Halide Perovskite $\text{CH}_3\text{NH}_3\text{PbI}_{3-x}\text{Cl}_x$. *J. Phys. Chem. Lett.* **2014**, *5*, 1300–1306.
- (45) Wu, K.; Bera, A.; Ma, C.; Du, Y.; Yang, Y.; Li, L.; Wu, T. Temperature-Dependent Excitonic Photoluminescence of Hybrid Organometal Halide Perovskite Films. *Phys. Chem. Chem. Phys.* **2014**, *16*, 22476–22481.
- (46) Wright, A. D.; Verdi, C.; Milot, R. L.; Eperon, G. E.; Pérez-Osorio, M. A.; Snaith, H. J.; Giustino, F.; Johnston, M. B.; Herz, L. M. Electron–Phonon Coupling in Hybrid Lead Halide Perovskites. *Nat. Commun.* **2016**, *7*, 11755.
- (47) Phuong, L. Q.; Braly, I. L.; Katahara, J. K.; Hillhouse, H. W.; Kanemitsu, Y. Nonlinear Photocarrier Recombination Dynamics in Mixed-Halide $\text{CH}_3\text{NH}_3\text{Pb}(\text{I}_{1-x}\text{Br}_x)_3$ Perovskite Thin Films. *Appl. Phys. Express* **2017**, *10*, 102401.
- (48) Handa, T.; Aharen, T.; Wakamiya, A.; Kanemitsu, Y. Radiative Recombination and Electron-Phonon Coupling in Lead-Free $\text{CH}_3\text{NH}_3\text{SnI}_3$ Perovskite Thin Films. *Phys. Rev. Mater.* **2018**, *2*, 75402.
- (49) Shum, K.; Chen, Z.; Qureshi, J.; Yu, C.; Wang, J. J.; Pfenninger, W.; Vockic, N.; Midgley, J.; Kenney, J. T. Synthesis and Characterization of CsSnI_3 Thin Films. *Appl. Phys. Lett.* **2010**, *96*, 3–5.
- (50) Milot, R. L.; Eperon, G. E.; Snaith, H. J.; Johnston, M. B.; Herz, L. M. Temperature-Dependent Charge-Carrier Dynamics in $\text{CH}_3\text{NH}_3\text{PbI}_3$ Perovskite Thin Films. *Adv. Funct. Mater.* **2015**, *25*, 6218–6227.

- (51) Straus, D. B.; Hurtado Parra, S.; Iotov, N.; Gebhardt, J.; Rappe, A. M.; Subotnik, J. E.; Kikkawa, J. M.; Kagan, C. R. Direct Observation of Electron–Phonon Coupling and Slow Vibrational Relaxation in Organic–Inorganic Hybrid Perovskites. *J. Am. Chem. Soc.* **2016**, *138*, 13798–13801.
- (52) Arend, T. R.; Tönnies, M.; Reisbeck, P.; Rieckmann, C. J. P.; Kersting, R. Physical Vapor Deposition of Methylammonium Tin Iodide Thin Films. *Phys. Status Solidi A* **2017**, *214*, 1600796.
- (53) Parrott, E. S.; Milot, R. L.; Stergiopoulos, T.; Snaith, H. J.; Johnston, M. B.; Herz, L. M. Effect of Structural Phase Transition on Charge-Carrier Lifetimes and Defects in $\text{CH}_3\text{NH}_3\text{SnI}_3$ Perovskite. *J. Phys. Chem. Lett.* **2016**, *7*, 1321–1326.
- (54) Klingshirn, C. F. *Semiconductor Optics*, 4th ed.; Springer, 2012.
- (55) Manser, J. S.; Kamat, P. V. Band Filling with Free Charge Carriers in Organometal halide Perovskites. *Nature Photonics* **2014**, *8*, 737–743.
- (56) Yang, Y.; Yan, Y.; Yang, M.; Choi, S.; Zhu, K.; Luther, J. M.; Beard, M. C. Low Surface Recombination Velocity in Solution-Grown $\text{CH}_3\text{NH}_3\text{PbBr}_3$ Perovskite Single Crystal. *Nat. Commun.* **2015**, *6*, 7961.
- (57) Ghosh, T.; Aharon, S.; Etgar, L.; Ruhman, S. Free Carrier Emergence and Onset of Electron–Phonon Coupling in Methylammonium Lead Halide Perovskite Films. *J. Am. Chem. Soc.* **2017**, *139*, 18262–18270.
- (58) Whalley, L. D.; Frost, J. M.; Morgan, B. J.; Walsh, A. Impact of Nonparabolic Electronic Band Structure on the Optical and Transport Properties of Photovoltaic Materials. *Phys. Rev. B* **2019**, *99*, 085207.